water

MDPI

Article

Baffle-Enhanced Scour Mitigation in Rectangular and Trapezoidal Piano Key Weirs: An Experimental and Machine Learning Investigation

Chonoor Abdi Chooplou [1], Ehsan Kahrizi [2], Amirhossein Fathi [1], Masoud Ghodsian [1] and Milad Latifi [3,*]

[1] Faculty of Civil and Environmental Engineering, Tarbiat Modares University, Tehran P.O. Box 14115-143, Iran; a.chonoor@modares.ac.ir (C.A.C.)
[2] Faculty of Civil and Environmental Engineering, Utah State University, Logan, UT 84322, USA; ehsan.kahrizi@usu.edu
[3] Centre for Water Systems, Faculty of Environment, Science and Economy, University of Exeter, Exeter EX4 4QF, UK
* Correspondence: m.latifi@exeter.ac.uk

Abstract: The assessment of scour depth downstream of weirs holds paramount importance in ensuring the structural stability of these hydraulic structures. This study presents groundbreaking experimental investigations highlighting the innovative use of baffles to enhance energy dissipation and mitigate scour in the downstream beds of rectangular piano key weirs (RPKWs) and trapezoidal piano key weirs (TPKWs). By leveraging three state-of-the-art supervised machine learning algorithms—multi-layer perceptron (MLP), extreme gradient boosting (XGBoost), and support vector regression (SVR)—to estimate scour hole parameters, this research showcases significant advancements in predictive modeling for scour analysis. Experimental results reveal that the incorporation of baffles leads to a remarkable 18–22% increase in energy dissipation and an 11–14% reduction in scour depth for both RPKWs and TPKWs. Specifically, introducing baffles in RPKWs resulted in a noteworthy 26.7% reduction in scour hole area and a 30.3% decrease in scour volume compared to RPKWs without baffles. Moreover, novel empirical equations were developed to estimate scour parameters, achieving impressive performance metrics with an average R^2 = 0.951, RMSE = 0.145, and MRPE = 4.429%. The MLP models demonstrate superior performance in predicting maximum scour depth across all scenarios with an average R^2 = 0.988, RMSE = 0.035, and MRPE = 1.036%. However, the predictive capabilities varied when estimating weir toe scour depth under diverse circumstances, with the XGBoost model proving more accurate in scenarios involving baffled TPKWs with R^2 = 0.965, RMSE = 0.048, and MRPE = 2.798% than the MLP and SVR models. This research underscores the significant role of baffles in minimizing scouring effects in TPKWs compared to RPKWs, showcasing the potential for improved design and efficiency in water-management systems.

Keywords: baffles; energy dissipation; machine learning methods; piano key weir; scour; outlet key

Citation: Abdi Chooplou, C.; Kahrizi, E.; Fathi, A.; Ghodsian, M.; Latifi, M. Baffle-Enhanced Scour Mitigation in Rectangular and Trapezoidal Piano Key Weirs: An Experimental and Machine Learning Investigation. *Water* **2024**, *16*, 2133. https://doi.org/10.3390/w16152133

Academic Editor: Giuseppe Pezzinga

Received: 5 July 2024
Revised: 19 July 2024
Accepted: 24 July 2024
Published: 27 July 2024

1. Introduction

Weirs are vital components of water transfer systems, frequently utilized in dams to control floods and regulate the water levels of reservoirs. They serve a critical function in managing flows within irrigation and drainage channels and accurately measuring discharges. Despite their significant utility, hydraulic structures like weirs are susceptible to a primary concern—local scouring, which threatens their stability and operational efficiency. Numerous studies have investigated the performance of piano key weirs (PKWs) in low-hydraulic-head conditions, where the complete aeration of flow can mitigate erosion and cavitation risks. However, as hydraulic heads increase, the advantages of PKWs diminish, impacting their overall effectiveness. Accurately estimating maximum scour

depth is essential for the safe and cost-efficient design of hydraulic structures to mitigate potential damage or failure [1]. Several scholars have contributed to understanding and predicting scour parameters downstream of PKWs under varying conditions, encompassing the geometric characteristics of scour holes and sediment ridges, energy dissipation rates, and the influence of different geometries on weir performance. In their comprehensive study, Jüstrich et al. [2] explored the impact of various parameters on the geometric features of scour holes and sediment ridges downstream of a RPKW, offering valuable insights and establishing predictive relationships for these parameters. Palermo et al. [3] observed that the equilibrium scour downstream of an RPKW is influenced by flow discharge, structure height, and tailwater depth. However, further analysis is required to fully comprehend the underlying physics and establish quantitative criteria for evaluating scour parameters. In their experiments, Kumar and Ahmad [4] investigated the scour patterns downstream of a three-cycle RPKW, with and without a solid apron. Their results indicated that scour was predominantly driven by jets originating from the keys. Deeper and longer scouring was observed for higher discharges and lower tailwater depths. Kumar et al. [5] examined the movement of sediment particles upstream of a RPKW and observed deceleration near the inlet keys followed by acceleration at the key ends. Ghodsian et al. [6] found that the maximum scour depth in a triangular PKW exceeded that of a trapezoidal PKW. Lantz et al. [7] experimentally explored the impact of apron configurations on downstream scour geometry under various hydraulic conditions, demonstrating the effectiveness of horizontal aprons in deflecting outflow plunging jets from an RPKW and significantly reducing scour depth. Further enhancing our understanding of scour mitigation strategies, Kumar and Ahmad [8] explored the impact of apron installations on scour downstream of RPKWs under free and submerged flow conditions, reporting significant scour depth reductions with the incorporation of an apron. Abdi Chooplou et al. [9] studied the temporal evolution of scour downstream of a TPKW and observed a significant increase in the dimensions of the scour hole during the initial stages of scouring. Lantz et al. [10] investigated the local scour process downstream of a type A RPKW in non-cohesive sediments, emphasizing the impact of hydraulic conditions on scour mechanisms. Abdi Chooplou et al. [11] found that the scour volume decreased with increasing relative tailwater depth downstream of a TPKW. Additionally, their study indicated that altering the shape of lateral walls crest downstream of a rectangular PKW could reduce scour depth and the extension of the scour hole [12]. Bodaghi et al. [13] explored the effect of submergence of a TPKW on downstream scouring, noting a decrease in maximum scour depth with higher submergence ratios. Abdi Chooplou et al. [14] compared scour parameters downstream of PKWs with different shapes, highlighting differences in scour depth, length, area, volume, and asymmetry index among rectangular, trapezoidal, and triangular PKWs. Fathi et al. [15] analyzed the impact of varying step configurations at the outlet keys of RPKWs on scour depth, finding that additional steps and smaller bed materials reduced sediment ridge height. Optimizing weir designs based on these insights can aid in mitigating downstream scouring. Kumar et al. [16] conducted a numerical study on the flow field and sediment passing capacity of type A RPKWs, revealing increased velocity components due to the vertical contraction in front of the sloped keys. This flow pattern has significant implications for sediment passing capacity and the overall performance of such hydraulic structures.

In a comparative analysis, Erpicum and Machiels [17] evaluated the energy dissipation rates between a RPKW and an Ogee spillway, revealing nearly equivalent levels of energy dissipation for both hydraulic structures. Additionally, Eslinger and Crookston [18] studied energy dissipation in RPKWs with varying geometries, highlighting the role of flow dynamics through the structure's front faces and upstream overhangs in facilitating energy dissipation. Naghibzadeh et al. [19] conducted experimental and numerical investigations on energy dissipation in RPKWs with stepped and baffled downstream slopes, uncovering a decrease in energy dissipation with increasing discharge. Notably, their study revealed that baffled PKWs exhibited more energy dissipation compared to

stepped and un-baffled PKWs. Delving into the performance aspects of PKWs, Souri et al. [20] conducted numerical simulations to evaluate the influence of aeration on both RPKW and TPKWs. Iqbal and Ghani [21] conducted a study on the energy dissipation characteristics of a PKW, analyzing the effects of varying key slope and key width ratios. Their findings revealed that an increase in key slope led to enhanced energy dissipation, whereas an increase in key width ratio resulted in reduced energy dissipation. Compared to traditional weirs, the PKW demonstrated superior energy dissipation, particularly evident at low flow rates.

The adoption of artificial neural networks (ANNs) and machine learning (ML) algorithms has emerged as a promising alternative to traditional regression models in predicting scour depth at hydraulic structures. These techniques exhibit strong generalization capabilities to unseen data and offer accurate predictions. Recent progress in hydraulic engineering has seen a notable increase in the use of ANNs and ML methods for precisely estimating scour depth at a range of hydraulic structures. Researchers have been dedicated to thoroughly assessing the effectiveness of different ML models in this crucial field. Muzzammil [22] showcased the remarkable capabilities of adaptive neuro-fuzzy inference systems (ANFIS) in modeling scour depth at bridge abutments, underscoring its superior predictive accuracy. Conversely, Najafzadeh et al. [23] demonstrated that the group method of data handling (GMDH) surpassed support vector machines (SVMs) in estimating scour depth around bridge abutments, highlighting the discerning nature of model selection in optimizing accuracy. Etemad-Shahidi et al. [24] reported the high fidelity of the M5 model tree in simulating scour depth around bridge piers, indicative of its robust predictive power. Similarly, Sharafi et al. [25] delineated the supremacy of SVM with diverse kernel functions over traditional methods like ANNs and ANFIS in forecasting scour depth around bridge piers, emphasizing the versatility of ML frameworks. Azimi et al. [26] innovatively integrated ANFIS-DE/SVD, a fusion of ANFIS and Differential Evolutionary algorithms, to outperform genetic algorithms (GAs) in simulating scouring around bridge pile groups, showcasing the promise of hybrid techniques. Additionally, Ebtehaj et al. [27] ascertained that extreme learning machines (ELM) outperformed SVM and ANN in providing precise forecasts of local scour depth around pile groups, heralding a new era of accuracy in scour depth estimation.

The advent of novel methodologies such as the self-adaptive extreme learning machine (SAELM) model, as demonstrated by Rashki-GhalehNou et al. [28], has pushed the boundaries of predictive accuracy beyond conventional models like ANN and SVM, particularly in predicting scour parameters downstream of sloping submerged weirs. Furthermore, Sharafati et al. [29] leveraged the optimization capabilities of ANFIS with innovative methods to predict scour depth downstream of sharp-crested weirs, revealing that ANFIS-IWO emerged as the most effective predictive model in this context. In an era characterized by the fusion of diverse computational techniques, Salih et al. [30] introduced the tBPSO-SVR model, a fusion of enhanced binary particle swarm optimization and support vector regression, as a potent tool for forecasting scour depth at submerged weirs, surpassing traditional methods like linear regression and decision trees. Moreover, the integration of ground penetrating radar (GPR), random forest (RF), and M5 tree models by Ahmadianfar et al. [31] through the least squares boosting ensemble showcased a synergistic approach to enhancing scour depth around pile groups estimation accuracy. Pandey et al. [32] further advanced the domain by employing ensemble-based techniques like categorical boosting (CatBoost), extra tree regression (ETR), and K-nearest neighbor (KNN) algorithms to predict scour depth around bridge abutments, with gradient boosting decision trees (GBDT) identifying crucial features for accurate modeling. Salmasi et al. [33] underscored the precision of gene expression programming (GEP) in predicting scouring induced by free fall jets, exemplifying the potential of innovative methodologies in scour parameter estimation. Iqbal and Ghani [34] demonstrated that artificial neural network (ANN) models can effectively forecast the discharge capacity of PKWs, surpassing the performance of conventional empirical equations. Their research involved the

creation of robust ANN models that exhibited strong correlations with experimental data, pinpointing the significant parameters that impact PKW discharge.

While advancements have been made in predicting scour parameters, a significant research gap exists in the exploration of energy dissipation and scour mitigation strategies specific to PKWs. This study aims to fill this crucial knowledge void by investigating the energy dissipation characteristics of type A RPKWs and TPKWs, assessing the effectiveness of baffle installations on outlet keys for mitigating downstream scour, and developing reliable machine learning models for accurately predicting local scour features downstream of baffled PKWs. By achieving these goals, this study will offer valuable insights into optimizing the performance and stability of PKWs through tailored scour prediction and mitigation strategies. This research directly addresses a critical need in hydraulic engineering and contributes to advancing more resilient and sustainable hydraulic structures through the innovative application of machine learning techniques.

2. Materials and Methods

2.1. Dimensional Analysis

The downstream scour phenomena of a PKW and the associated key parameters are illustrated in Figure 1. In this representation, key variables include the upstream total head H ($=h_u + V_0^2/2g$, h_u is upstream depth of flow relative to the weir crest, V_0 is approach flow velocity, g is gravitational acceleration), h_d signifies the depth of the tailwater, H_d characterizes the downstream head, ΔH indicates the difference between the upstream and downstream heads, Z_{SF} depicts the scour depth at the weir toe, d_{SM} represents the maximum scour depth, X_{SM} designates the distance from the weir toe to the location of maximum scour depth, and L_S represents the length of the scour hole.

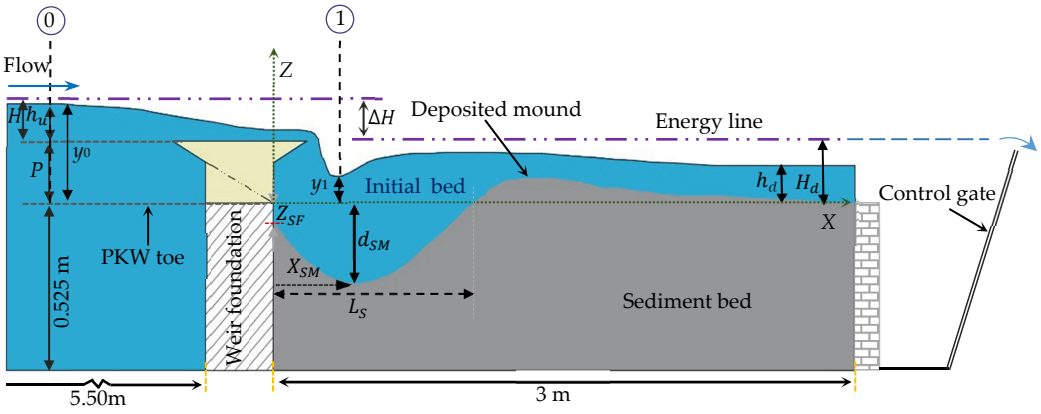

Figure 1. Flow and scour parameters at PKW.

The components of a type A PKW outlined in Figure 2 encompass the following parameters: the length of the weir crest (L), the height of the weir (P), the width of the weir (W), the width of the inlet key (W_i), the width of the outlet key (W_o), the streamwise length of the weir (B), the base length of the weir (B_b), the lengths of the inlet and outlet keys overhang (B_i and B_o, respectively), the width of the weir cycle (W_u), and the thickness of the weir wall (T_s).

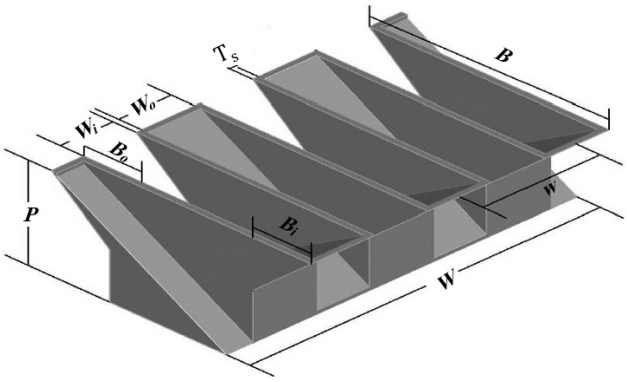

Figure 2. Geometric parameters of a PKW.

Various factors affecting the scoring downstream of a PKW include the flow characteristic (f_{Flow}), the properties of the bed materials and water ($f_{Bed,\ Water}$), the geometric parameters of the PKW ($f_{Geometry}$), and the presence of baffles ($f_{baffles}$):

$$\Psi = f\left\{\begin{matrix} f_{Flow}(V_j, h_u, H, \Delta H, h_d),\ f_{Bed,\ Water}(d_{50}, \rho_w, \rho_s, g),\ f_{Geometry}(P, W_i, W_o, W, B_i, B_o, \\ B_b, B, T_S, N, \zeta),\ f_{Baffles}(H_B) \end{matrix}\right\} \quad (1)$$

here ψ denotes the dimensions of the scour hole and sedimentary ridge, f is the function symbol, V_j $(= \sqrt{2g\Delta h})$ signifies the velocity of the jet at the tailwater level, d_{50} denotes the mean sediment size, ρ_w denotes the density of water, ρ_s represents the density of sediment, N signifies the number of weir cycles, ζ denotes the effect of the weir's shape, and H_B indicates the height of the baffles. By utilizing the Buckingham Π theorem, and subsequently combining dimensionless parameters while excluding constant factors, the following equation is derived for a baffled PKW:

$$\frac{\Psi}{H} = f\left(\mathrm{Fr}, \frac{\Delta H}{h_d}, \zeta, \frac{h_u}{H_B}\right) \quad (2)$$

where Fr $(= V_j/\sqrt{gh_d})$ is the Froude number.

2.2. Experiments

2.2.1. Experimental Setup

The tests were carried out in a rectangular channel with 10 m length, 0.75 m width, 0.80 m height, and a longitudinal bed slope of 0.001, in the hydraulic laboratory of the water engineering and hydraulic structures group at Tarbiat Modares University in Tehran. The channel's walls were constructed from glass, while the bottom was made of metal. A pump capable of supplying water at a maximum rate of 0.085 m^3/s transported water from a sump to the channel.

Tailwater depth adjustments were facilitated by a gate situated at the channel's endpoint. All experiments were conducted under free-flow conditions. The viscosity effects are negligible in turbulent flow with Reynolds numbers greater than 30,000 [35,36]. As recommended by Pfister et al. [37] and Erpicum et al. [38], a minimum upstream depth of $H \geq 0.03$ m was ensured. Additionally, to mitigate the influence of surface tension, the ratio of H/P was kept above 0.1 [39]. The initial level of the sediment bed in all experiments was equal to the weir toe level. A thin metal sheet was placed over the sediments to prevent the start-up effect.

2.2.2. Experimental Layout and Parameters

Based on established guidelines by Lempérière and Ouamane [40]; Lempérière and Jun [41], and Mehboudi et al. [42], two distinct geometrical configurations of PKWs were

used in the experiments: rectangular and trapezoidal shapes (Figure 3). The PKWs featured three cycles ($N = 3$) and were manufactured using thermoplastic material through a three-dimensional printing process. They were positioned approximately 3 m from the entrance of the channel. Detailed specifications of the PKWs, including the sidewall angle denoted as α, are provided in Table 1.

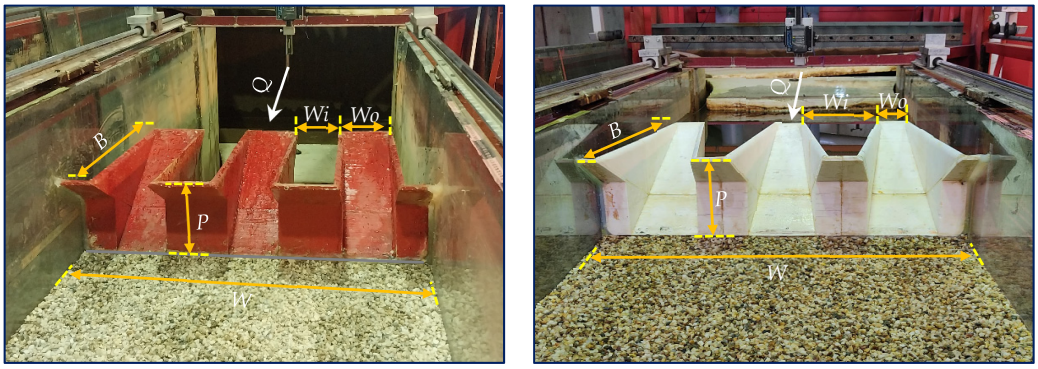

(**a**) (**b**)

Figure 3. Downstream view of: (**a**) RPKW and (**b**) TPKW.

Table 1. Dimensions of used PKWs.

P (m)		0.20	B_b (m)	0.25
L (m)	RPKW	3.75	B_i (m)	0.125
	TPKW	3.30	B_o (m)	0.125
W_i (m)	RPKW	0.125	W (m)	0.75
	TPKW	0.175		
W_o (m)	RPKW	0.125	T_s (m)	0.012
	TPKW	0.051		
α (degree)	RPKW	0	N (-)	3
	TPKW	5		

The study employed a non-cohesive quartz gravel bed with a median size (d_{50}) of 7.1 mm to induce scouring, ensuring uniformity with a standard deviation (σ_g) of less than 1.5, adhering to recommendations from previous studies [43,44]. The tested range of d_{50}/P values in this investigation was aligned with typical prototype conditions, with weir heights (P) varying from 3.0 m to 5.0 m, consistent with studies by *Ho* Ta Khanh et al. [45] and Laugier et al. [46]. This alignment indicates the generalizability of the results to coarse river beds, as supported by the work of Jüstrich et al. [3]. Additionally, the negligible scale effect on scouring was validated by the d_{10} value (5.2 mm) exceeding the recommended threshold of 1.0 mm, as advised by Pagliara et al. [47].

A 3 m long and 0.75 m wide area downstream of the PKW was covered with sediments and leveled using a bed leveler (Figure 4). To prevent sediment intrusion into the sump, a metal mesh was strategically installed at the channel's end.

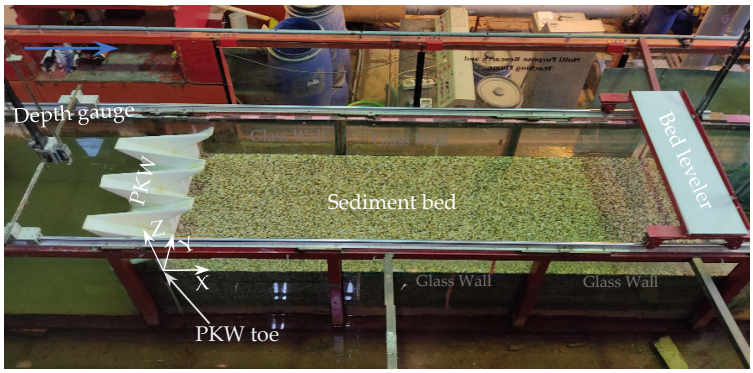

Figure 4. PKW and downstream sediment bed.

The baffles, constructed from coated wood in a cubic shape, were designed as per the recommendations of the United States Bureau of Reclamation [48]. The baffles' height was fixed at 0.032 m, with a longitudinal spacing of 0.064 m (equal to 2 times the baffle height). The longitudinal base width of the baffles matched the outlet keys, set at 0.026 m. Figure 5 shows the details and layout of the baffles implemented on the outlet keys.

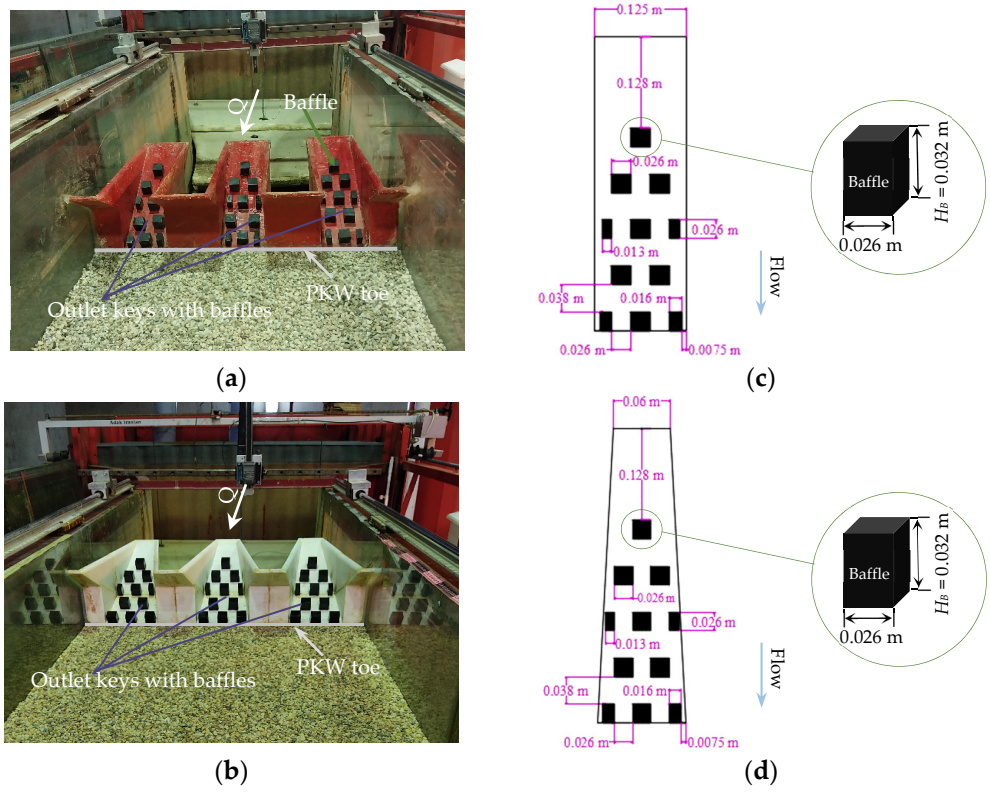

Figure 5. Baffles in PKW outlet keys: (**a**,**b**) photo from downstream of RPKW and TPKW; (**c**,**d**) dimensions and layout of RPKW and TPKW.

2.2.3. Test Details and Summary

Table 2 contains a comprehensive summary of the tests, consisting of 80 experiments. The symbol *B*(*Q*)-(*hd*) denotes the tested model, with "*B*" denoting the series of tests involving baffled weirs. The first numeric element represents the discharge in liters per second, accompanied by the tailwater depth indicated in centimeters. The experiments covered discharges ranging from 0.03 to 0.06 m^3/s, relative drop heights ($\Delta H/h_d$) spanning from 0.26 to 1.74, and Froude numbers (Fr) between 0.74 and 2.12.

Table 2. Details of the experiments.

Sl. No	Tests	Q	h_d	PKW	Fr	$\Delta H/h_d$	h_u/H_B	Sl. No	PKW	Fr	$\Delta H/h_d$	h_u/H_B
#	#	m^3/s	m	#	-	-	-	#	#	-	-	-
1	30-8	0.30	0.08	RPKW	1.93	1.70	-	41	TPKW	1.95	1.74	-
2	B30-8						1.00	42				0.91
3	30-10		0.10		1.61	1.21	-	43		1.62	1.24	-
4	B30-10						1.00	44				0.91
5	30-13		0.13		1.23	0.72	-	45		1.25	0.75	-
6	B30-13						1.00	46				0.91
7	30-15		0.15		1.03	0.50	-	47		1.05	0.52	-
8	B30-15						1.00	48				0.91
9	30-18		0.18		0.74	0.26	-	49		0.76	0.27	-
10	B30-18						1.00	50				0.91
11	40-8	0.04	0.08		1.98	1.68	-	51		2.00	1.72	-
12	B40-8						1.25	52				1.16
13	40-10		0.10		1.66	1.23	-	53		1.67	1.26	-
14	B40-10						1.25	54				1.16
15	40-13		0.13		1.28	0.76	-	55		1.30	0.78	-
16	B40-13						1.25	56				1.16
17	40-15		0.15		1.08	0.54	-	57		1.10	0.56	-
18	B40-15						1.25	58				1.16
19	40-18		0.18		0.80	0.29	-	59		0.82	0.31	-
20	B40-18						1.25	60				1.16
21	50-8	0.05	0.08		2.05	1.66	-	61		2.06	1.68	-
22	B50-8						1.56	62				1.50
23	50-10		0.10		1.72	1.22	-	63		1.73	1.27	-
24	B50-10						1.56	64				1.50
25	50-13		0.13		1.35	0.80	-	65		1.36	0.82	-
26	B50-13						1.56	66				1.50
27	50-15		0.15		1.14	0.59	-	67		1.15	0.60	-
28	B50-15						1.56	68				1.50
29	50-18		0.18		0.87	0.34	-	69		0.88	0.35	-
30	B50-18						1.56	70				1.50
31	60-8	0.06	0.08		2.11	1.59	-	71		2.12	1.61	-
32	B60-8						1.88	72				1.81
33	60-10		0.10		1.78	1.25	-	73		1.79	1.27	-
34	B60-10						1.88	74				1.81
35	60-13		0.13		1.40	0.84	-	75		1.41	0.85	-
36	B60-13						1.88	76				1.81
37	60-15		0.15		1.20	0.62	-	77		1.21	0.64	-
38	B60-15						1.88	78				1.81
39	60-18		0.18		0.93	0.38	-	79		0.94	0.39	-
40	B60-18						1.88	80				1.81

The largest tested unit discharge (q = 0.08 m^2/s) in the study corresponds to approximately 23 m^2/s in the prototype condition. This value was obtained using a scale factor of 40, as reported by Dugué et al. [49].

2.2.4. Experimental Measurements

The measurement procedures encompassed the use of several sophisticated instruments. The upstream flow depth and tailwater depth were ascertained using a digital point gauge, boasting an accuracy of ±1 mm. The discharge was measured using a calibrated ultrasonic flow meter (Model TFM3100-F1) with ±1% accuracy, attached to the inflow pipe. To accommodate the formation of a hydraulic jump downstream of the weirs, downstream velocity was computed utilizing the flow depths measured before the jump. As the flow was notably three-dimensional, multiple depth measurements were conducted and subsequently averaged to determine the downstream velocity. The experiment commenced by gradually removing the metal sheet to minimize its influence on the sediment bed. Each test recorded the discharge, as well as the upstream and downstream flow depths around the PKWs. After reducing the discharge and draining the channel bed, the bed topography was meticulously documented using a laser bed profiler.

To ascertain the equilibrium time, a 15 h test was conducted to observe scour depths, as illustrated in Figure 6, which captured the most critical state characterized by the highest discharge (Q = 0.06 m^3/s) and lowest tailwater depth (h_d = 0.08 m). Clear from the graph, after roughly 180 min into the experiment, the increase in scour depth became negligible, aligning with the criteria outlined by Chiew [50] and Kumar et al. [51] for the equilibrium state. As such, the duration of 180 min was adopted as the equilibrium state for subsequent experiments. Additionally, the tests revealed a progressive increase in the local scour depth downstream of the weir in the absence of baffles in the outlet keys, peaking after 180 min as the system attained an equilibrium state—a trend in line with prior studies on abutment scour [52].

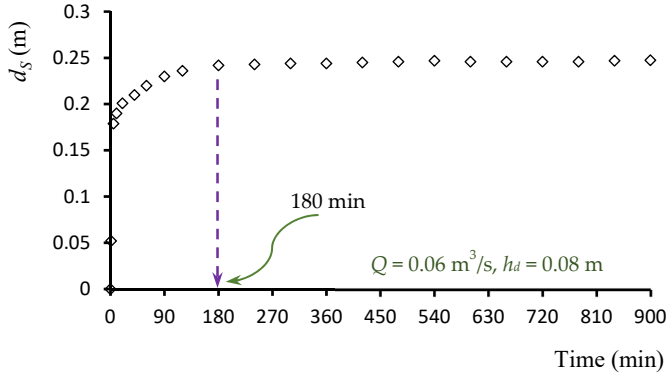

Figure 6. Temporal evolution of the scour depth for TPKW.

2.3. Machine Learning Algorithms

2.3.1. Extreme Gradient Boosting—Skopt

Extreme gradient boosting—skopt (XGBoost) is a powerful machine learning method that combines predictions from multiple weak models to enhance overall prediction accuracy. It employs gradient boosting, an iterative process that fits weak models to the negative gradient or residual of the previous iteration. By utilizing first- and second-order gradients, XGBoost captures the curvature of the loss function. Regularization techniques (such as L1 and L2) penalize complex models to improve generalization. Additionally, XGBoost incorporates optimizations like parallel processing and cache awareness for efficient computation [53].

This study employs the *XGBoost* algorithm using the XGBRegressor from the *xgboost* library, combined with a grid search (*GridSearchCV*) for optimizing hyperparameters such as *n_estimators*, *learning_rate*, *max_depth*, subsample, and *colsample_bytree*. The algorithm's steps are shown in Figure 7.

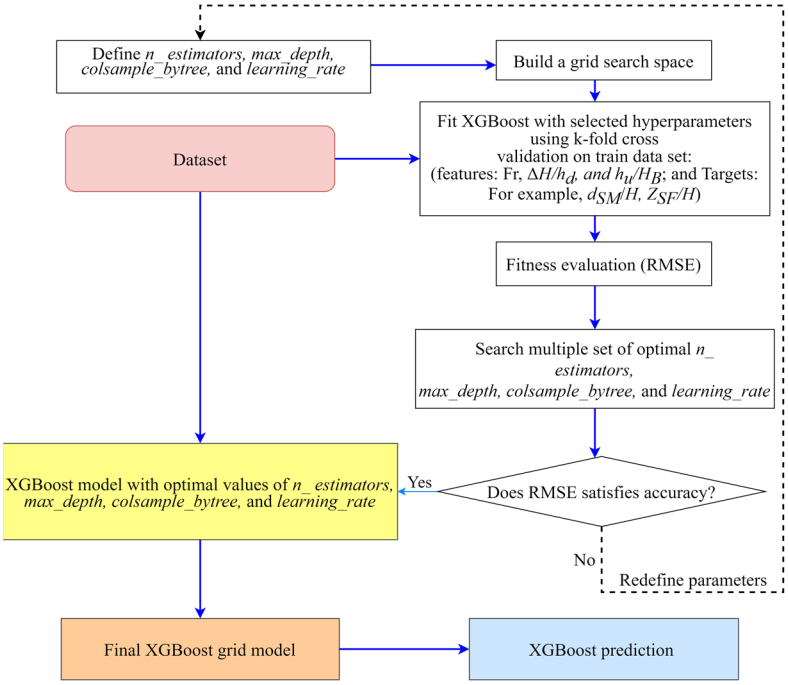

Figure 7. Flowchart of the XGBoost technique.

2.3.2. Multi-Layer Perceptron (MLP)—Hyperopt Optimizer

The MLP is a feed-forward algorithm that was developed to address the limitation of the perceptron, as highlighted by Minsky and Papert [54], which cannot handle non-linear data with just one neuron. The MLP includes input and output layers, as well as one or more hidden layers containing multiple neurons. Neurons in the MLP require an activation function, such as the ReLU function, to set a threshold, which is calculated using a specific equation:

$$\mathrm{ReLU}(x) = \max(0, x) \tag{3}$$

where x is the input variable.

The MLP integrates inputs with initial weights, applies an activation function, and passes the outcomes to the following layer. This process repeats through the hidden layers until it reaches the output layer [55].

Figure 8 depicts a hypothetical structure of an MLP model. The MLP model used in this paper has more nodes than displayed in Figure 8. Here, w_{11} to w_{33} and v_{11} to v_{31} display weights, and the output variable (y) illustrates different relative scour parameters such as d_{SM}/H and Z_{SF}/H.

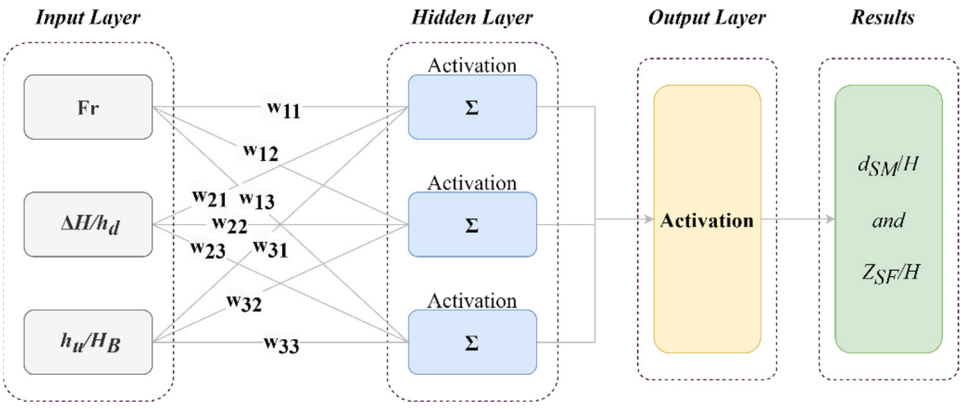

Figure 8. The structure of an MLP model.

To create MLP models for this study, the *MLPRegressor* class from the sklearn library was utilized with its default parameters, including a batch size of 4. The Sgd and Ilfgs solver were employed, and MSE was used as the loss function. Only two hyperparameters, namely the number of neurons in the hidden layer (*hidden_layer_sizes*) and the maximum number of iterations (*max_iter*), were tuned to find the optimal model. The regularization parameters C, ε, and γ in the model play crucial roles in balancing complexity and accuracy. Increasing C emphasizes minimizing training errors, potentially leading to overfitting. Reducing C prevents overfitting and enhances generalization. ε determines the acceptable error level, with higher values promoting flexibility and lower values prioritizing precision [56]. γ influences the support vectors' radius, with higher values capturing intricate patterns and lower values focusing on broader trends [57].

2.3.3. The Support Vector Regression (SVR)

The SVR is a precise machine learning algorithm commonly used for regression purposes. The specifics of this algorithm can be referenced in the works of Ceperic et al. [58]. When developing SVR models to predict scour hole characteristics downstream of a TPKW, the SVR class from the *sklearn* library is typically used with its default settings. The only parameter that needs to be adjusted is the kernel, which should be set to the radial basis function (RBF) type, and three key *hyperparameters* of the fine-tuned SVR.

The regularization parameter C plays a crucial role in balancing the complexity of the model with the desired accuracy of the training data. By increasing C, the emphasis shifts towards minimizing training errors, which could lead to a more complex and potentially overfitting model. Conversely, reducing C can help prevent overfitting and enhance the model's ability to generalize to unseen data [56]. The ε parameter establishes the acceptable error level for the model and can be assigned decimal values. A higher ε value promotes a more flexible model that can accommodate outliers or noisy data, possibly sacrificing precision. Conversely, a lower ε value results in a more precise model that focuses on error minimization, potentially neglecting outliers or noisy data [56]. The γ parameter determines the support vectors' influence radius. Increasing γ enables the model to capture intricate patterns in the training data, potentially at the expense of generalization to unseen data. Conversely, decreasing γ encourages a more generalized representation of the data, allowing the model to focus on capturing broader patterns and trends [57].

2.4. Model Development

This section details the development of machine learning models to predict scour hole characteristics downstream of a trapezoidal and rectangular PKW. Three primary models are constructed, XGBoost, MLP, and SVR models, which will be elaborated on in the subsequent sections.

2.4.1. Data Processing

Data preprocessing involves preparing data for algorithms. Initially, the data were divided into training and testing datasets using the hold-out strategy, where 80% of the data were allocated for training, and the remaining 20% were reserved for testing [59]. This split was accomplished using the *train_test_split* function from the Python sklearn library, with a *test_size* of 0.2. For modeling the relative toe scour depth (Z_{SF}/H) and the relative maximum scour diameter (d_{SM}/H), the training set consisted of 64 samples, and the testing set had 16 samples.

The MLP model benefits from normalizing input features. Failure to do so can result in longer convergence times or even failure to converge. To address this, the *MinMaxScaler* class from *sklearn* was used to normalize both training and testing datasets, ensuring all features were on a similar scale.

2.4.2. Hyperparameter Optimization

XGBoost: The hyperparameter optimization for the *XGBoost* model utilizes the Bayesian optimization algorithm provided by the '*skopt*' library, specifically the *gp_minimize* function. This optimizer uses Gaussian processes to model the function we aim to minimize, which is the root mean squared error (RMSE) in this case. The optimization process involves defining a search space for hyperparameters such as *n_estimators* (ranging from 100 to 1000), *learning_rate* (0.01 to 0.3), *max_depth* (3 to 10), *subsample* (0.6 to 1.0), *colsample_bytree* (0.6 to 1.0), *gamma* (0.0 to 1.0), and *min_child_weight* (1 to 10).

The objective function trains the XGBoost model with the given hyperparameters, evaluates its performance on a test set, and returns the RMSE. The optimizer iteratively explores the hyperparameter space to identify the combination that minimizes the RMSE, improving predictive performance and ensuring efficient convergence. The *CheckpointSaver* callback is used to save the optimizer's progress and state, ensuring that results are not lost in case of interruptions. After 100 iterations, the best hyperparameters are identified and used to train the final XGBoost model, which is then evaluated using metrics such as R^2, RMSE, and MRPE on both training and testing datasets. The detailed hyperparameter values are presented in Table 3.

Table 3. The structure of the developed XGBoost model.

Model	Hyperparameter Optimizer	Dataset	n_Estimators	Learning_Rate	Max_Depth	Subsample	Colsample_Bytree	Gamma	Min_Child_Weight
XGBoost	Scikit-Optimize (skopt)	d_{SM}/H_RPKW, (un-baffled)	100.000	0.300	9.000	0.987	0.770	1.000	1.000
		d_{SM}/H_RPKW, (baffled)	328.000	0.010	9.000	0.600	0.600	0.108	1.000
		d_{SM}/H_TPKW, (un-baffled)	1000.000	0.010	3.000	1.000	0.637	0.360	1.000
		d_{SM}/H_TPKW, (baffled)	100.000	0.044	6.000	1.000	0.655	0.000	1.000
		Z_{SF}/H_RPKW, (un-baffled)	1000	0.300	3.000	0.914	1.000	0.4231	2.000
		Z_{SF}/H_RPKW, (baffled)	358	0.300	6.000	0.6	0.789	0.000	3.000
		Z_{SF}/H_TPKW, (un-baffled)	888	0.1942	6.000	0.814	0.990	0.1548	8.000
		Z_{SF}/H_TPKW, (baffled)	527	0.300	3.000	0.980	1.000	0.079	3.000

The *MLP* model uses the Tree-structured Parzen Estimator (TPE) algorithm from Hyperopt to optimize hyperparameters. The goal is to minimize the root mean squared error (RMSE) by adjusting parameters such as hidden layer sizes, activation functions, solvers, and regularization parameters. The process involves defining a search space, performing 100 evaluations, and tracking performance metrics to select the best hyperparameters. The selected hyperparameters are used to train the final *MLP* model, which is then evaluated on both training and testing datasets using relevant metrics. The detailed hyperparameter values are presented in Table 4.

Table 4. The structure of the developed MLP model.

Model	Hyperparameter Optimizer	Dataset	Hidden Layer Sizes	Alpha	Momentum	Beta 1	Beta 2
MLP	Hyperopt TPE (Tree-structured Parzen Estimators)	d_{SM}/H_RPKW, (un-baffled)	(100, 100)	0.000750926	0.9561	0.9987	0.9423
		d_{SM}/H_RPKW, (baffled)	(100, 100)	0.003859803	0.9127	0.9606	0.9546
		d_{SM}/H_TPKW, (un-baffled)	(100, 50)	0.000247312	0.9556	0.9914	0.9875
		d_{SM}/H_TPKW, (baffled)	(50, 50)	0.002464564	0.9457	0.9711	0.9673
		Z_{SF}/H_RPKW, (un-baffled)	(100, 100)	0.005015594	0.9179	0.9686	0.9595
		Z_{SF}/H_RPKW, (baffled)	(100,)	0.000176462	0.9123	0.9042	0.9673
		Z_{SF}/H_TPKW, (un-baffled)	(150,)	0.001310837	0.9498	0.9223	0.9525
		Z_{SF}/H_TPKW, (baffled)	(150, 100)	0.000111521	0.9183	0.9147	0.9774

The *SVR* model uses GridSearchCV to optimize hyperparameters. It evaluates a range of values for *C* (1–10,000), gamma (0.005–100), and epsilon (0.01–0.25) using a 5-fold

cross-validation. The goal is to minimize the mean squared error (MSE) of predictions. The best model, determined by the lowest RMSE, is used to predict outcomes on both training and testing datasets. The structure of the SVR model in different cases is shown in Table 5.

Table 5. The structure of the developed SVR model.

Model	Hyperparameter Optimizer	Dataset	*C*	Gamma	Epsilon	Degree
SRV	GridSearchCV	d_{SM}/H_RPKW, (un-baffled)	9899	0.005	0.19	3
		d_{SM}/H_RPKW, (baffled)	3031	0.005	0.25	3
		d_{SM}/H_TPKW, (un-baffled)	102	50.00	0.01	3
		d_{SM}/H_TPKW, (baffled)	9899	0.005	0.07	3
		Z_{SF}/H_RPKW, (un-baffled)	203	0.005	0.07	3
		Z_{SF}/H_RPKW, (baffled)	102	0.005	0.01	3
		Z_{SF}/H_TPKW, (un-baffled)	9293	0.005	0.07	3
		Z_{SF}/H_TPKW, (baffled)	102	0.005	0.01	3

3. Results and Discussion

3.1. Experimental Data Evaluation

In this research, the characteristics of scour holes downstream of PKWs were evaluated to investigate the effects of baffles in the weir outlet keys under different hydraulic conditions. Figure 9 illustrates the flow patterns for PKWs with and without baffles. During the tests, two types of flows were observed in the inlet and outlet keys. The inlet keys drew the approaching flow towards themselves, which then discharged over the downstream crest as a falling jet. In contrast, the flows over the outlet keys were discharged as an inclined jet over the downstream sloped part of the weir. The water level rose in the outlet keys due to flow interference caused by the falling jet from the weir lateral walls with the upstream flow, resulting in severe flow turbulence.

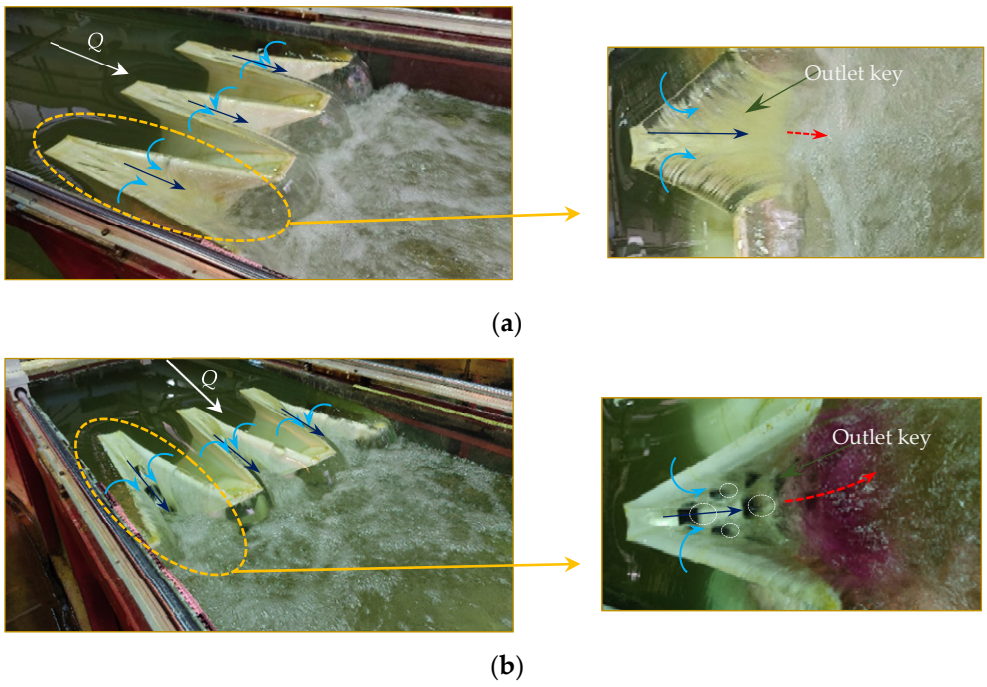

Figure 9. Flow over TPKW: (**a**) without baffles and (**b**) with baffles.

The flow surface downstream of the baffled weir was observed to rise with enhanced turbulence, which exhibited a highly three-dimensional nature. This is because the baffles

throw the water upwards, downstream of the outlet keys. Figure 10 compares the schematic flow patterns over baffled and un-baffled weirs. The impinging jet in the un-baffled weir (Figure 10a) transformed into a surface jet in the baffled weir (Figure 10b). Additionally, the interference between flow layers increased, and air entrainment was enhanced in the baffled weir. Furthermore, the friction and drag forces acting on the baffles, coupled with the low-pressure zone formed behind them, resulted in increased energy dissipation.

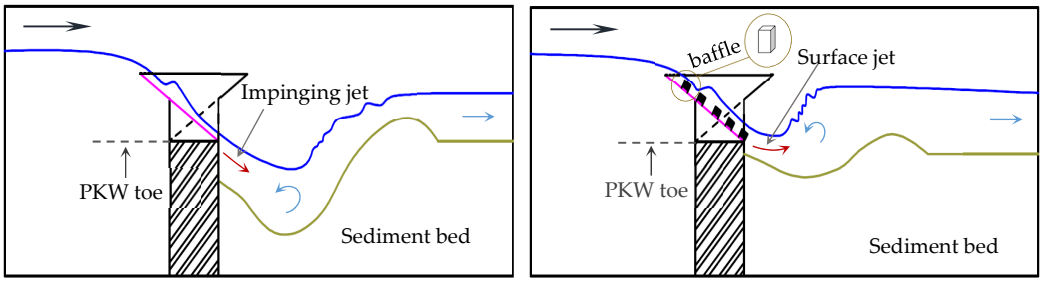

(**a**) (**b**)

Figure 10. Schematic of flow pattern along outlet keys in the weir: (**a**) without baffles and (**b**) with baffles.

The amounts of upstream specific energy E_0, downstream specific energy E_1, and relative energy loss ΔE are calculated by Equations (4)–(6). The percentage difference of energy loss for the baffled and un-baffled weirs ΔE_d was calculated using Equation (7).

$$E_0 = y_0 + \frac{V_0^2}{2g} \quad (4)$$

$$E_1 = y_1 + \frac{V_1^2}{2g} \quad (5)$$

$$\Delta E = \frac{E_0 - E_1}{E_0} \quad (6)$$

$$\Delta E_d = \frac{\Delta E_{baffled} - \Delta E_{un-baffled}}{\Delta E_{un-baffled}} \times 100 \quad (7)$$

where y_0 and y_1 are the flow depths upstream (=h_u + P) and downstream (=h_d + P) of the weir concerning initial bed level, respectively (Figure 1), V_1 represents the flow velocity downstream of the weir, and $\Delta E_{\text{baffled}}$ and $\Delta E_{\text{un-baffled}}$ are relative energy loss for baffled and un-baffled weirs, respectively.

Figure 11 shows a comparison of the difference in relative energy loss for the RPKW and TPKE with and without the baffles. As can be seen in Figure 11, the presence of baffles in the weir outlet key has increased the energy losses for all the models. The average energy loss in the RPKW and TPKW with baffles is significantly higher than that of the weir without baffles, with increases of approximately 18 and 22%, respectively. Furthermore, it is observable in both weir geometries that at a constant relative tailwater depth (h_d/P), the percentage differences in energy loss (ΔE_d) are more pronounced at lower Froude numbers, and these differences diminish as the Froude number increases. The influence of baffles on flow characteristics is more pronounced at lower Froude numbers, which correspond to lower flow depths (and lower h_u/H_B ratios). In this scenario, more layers of flow are affected by the baffles, as illustrated in Figure 12a, resulting in higher energy dissipation. Conversely, as the Froude number increases and the h_u/H_B ratio enhances, the vortex flows created in the separation region, based on the theory of falling flow (non-slip), prevent the full contact of flow with the baffles. Consequently, the effects of baffles on flow resistance decrease, and they only influence the lower layers of the flow (Figure 12b), thereby reducing the overall energy loss.

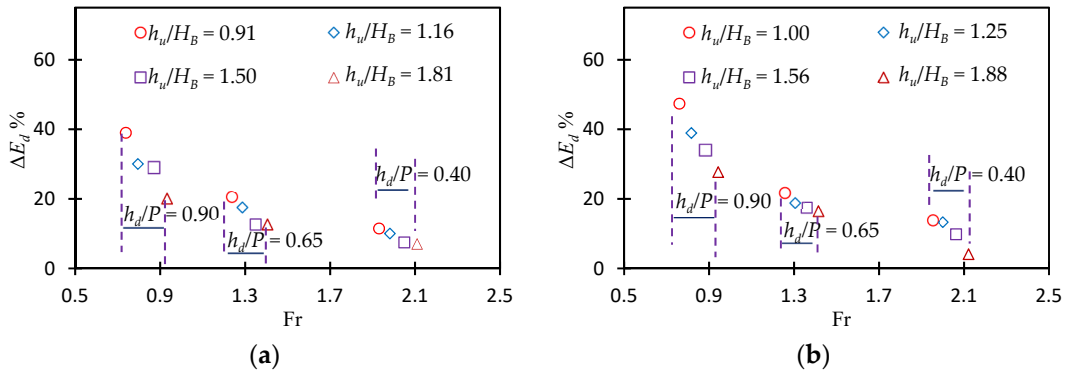

Figure 11. The difference of relative energy loss for weirs with and without baffles for: (**a**) RPKW and (**b**) TPKW.

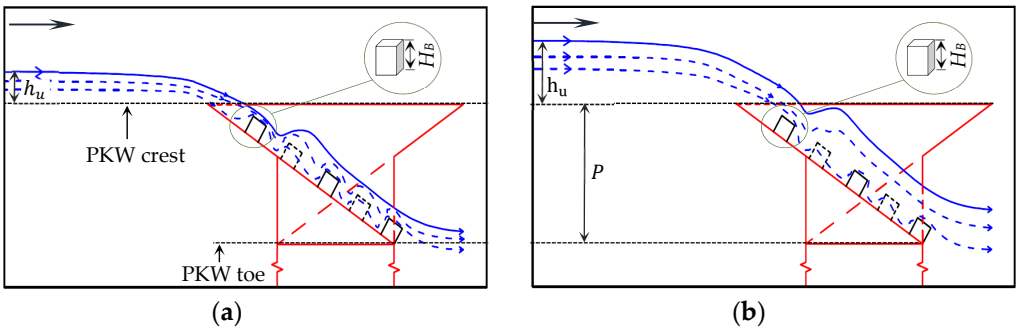

Figure 12. Schematic of the baffles effects on the flow layers with: (**a**) h_u/H_B = 1.00 and (**b**) h_u/H_B = 1.88.

Figure 13 compares the temporal variations of scour depth for weirs with and without baffles. In this figure, *t* represents the time of scouring, and *te* denotes the equilibrium time. The scour rate is high initially but decreases to an insignificant level by the end of the tests. The presence of baffles reduces the scour depth and its temporal variations. Increasing $\Delta H/h_d$ and Fr leads to an increase in scour depth. The results show that 80% of scouring occurs within the first hour. For the range of $0.75 \leq \Delta H/h_d \leq 0.85$, 73–87% of scour depth development occurs in the initial 30% of the test duration. The reducing effect of baffles on scour depth becomes more pronounced as the relative drop height decreases. At the equilibrium state, baffled weirs exhibit average scour depths that are 6.5, 15 and 15.5% less than those without baffles for the respective drop height ranges of $1.61 \leq \Delta H/h_d \leq 1.74$, $0.75 \leq \Delta H/h_d \leq 0.85$ and $0.27 \leq \Delta H/h_d \leq 0.39$ [Figure 13a–c].

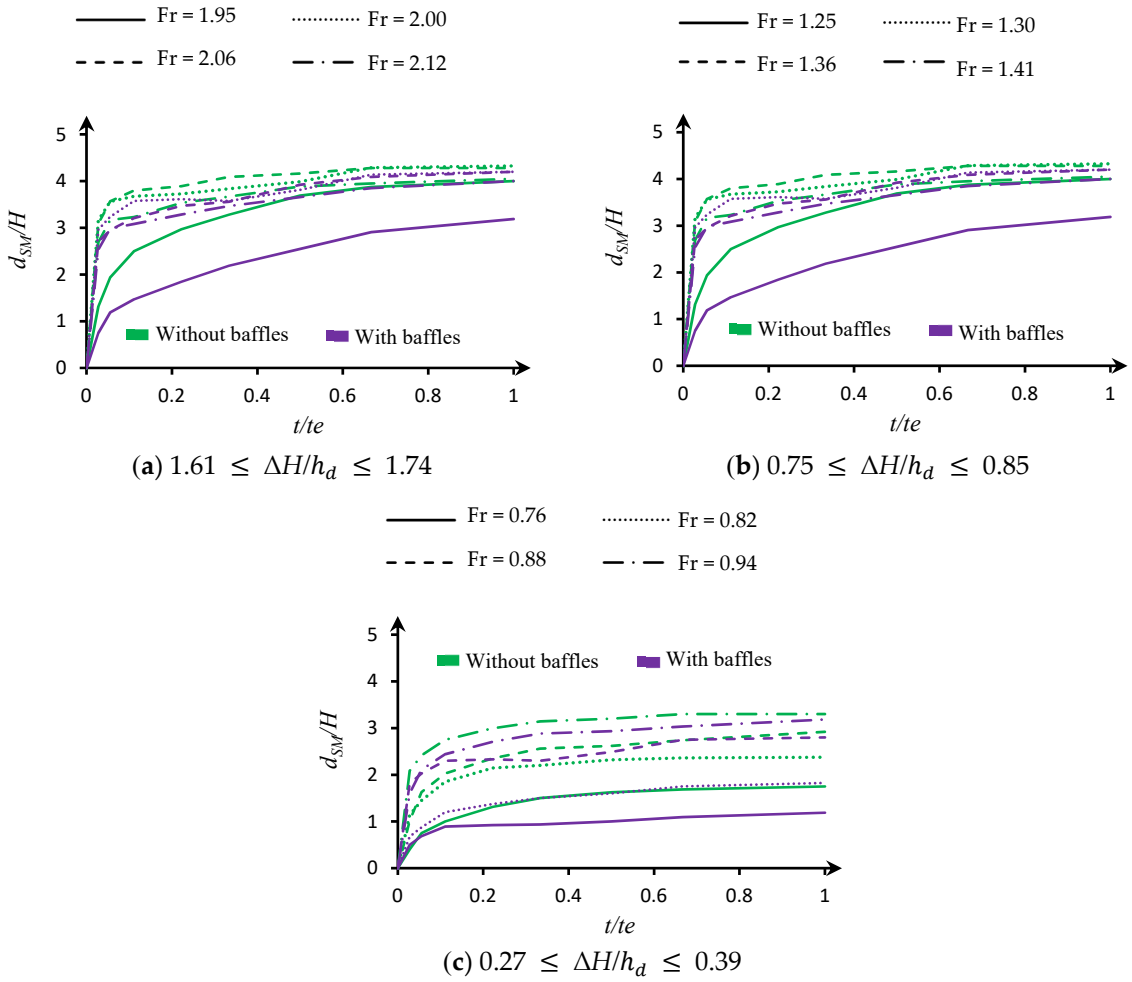

Figure 13. Temporal variations of the scour depth in the tests with and without baffles.

This study examined the changes in bed topography downstream of a weir, with and without the presence of baffles, under various Froude numbers and relative tailwater depths (Figure 14). The results indicate that increasing the Froude number and relative drop height increases the erosive power and sediment transfer downstream, while the presence of baffles reduces the topographical changes and limits the scour hole extension, with the smallest scour hole observed at Fr = 1.25 and $\Delta H/h_d$ = 0.75, resulting in a 21% reduction in scour. However, the difference in bed topography changes between baffled and un-baffled weirs decreased at the higher Froude numbers due to increased baffle resistance, and at the minimum Froude number, the baffled weir exhibited more flow interference and air entrainment, leading to less pronounced bed topography variations compared to the un-baffled configuration. The findings provide valuable insights into the role of baffles in modulating bed topography changes under varying hydraulic conditions, which can inform the design and optimization of weir structures for improved sediment management and environmental sustainability.

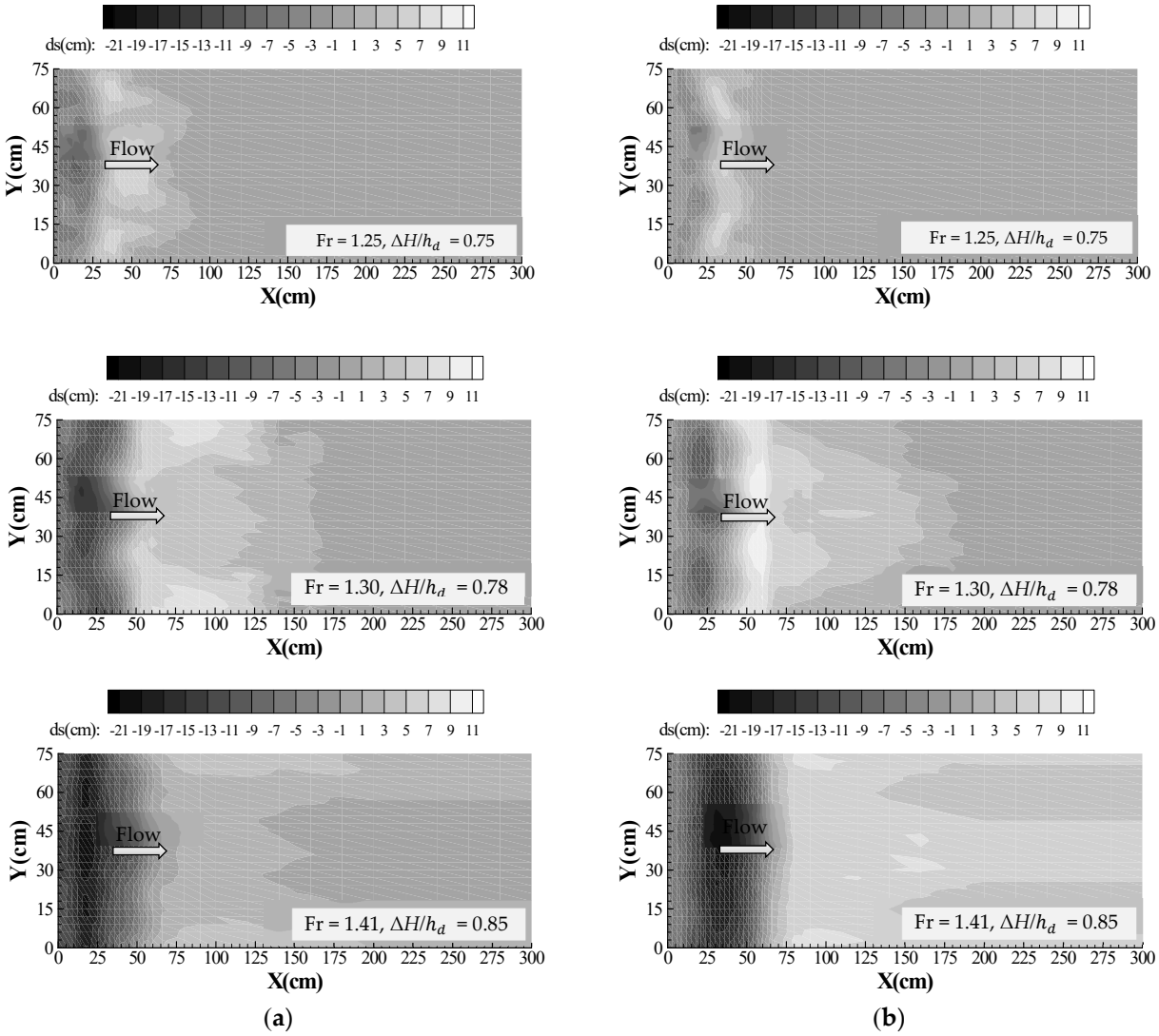

Figure 14. Typical downstream bed topography in the TPKW: (**a**) without baffles and (**b**) with baffles.

The effects of Froude number and relative drop height on the longitudinal bed profiles for the weirs with and without baffles are compared in Figure 15. This figure corresponds to the section with the deepest scour depth, which is downstream of outlet keys. According to this figure, the maximum scour depth at the baffled TPKW is, on average, 14% less than that of the un-baffled weir. The greatest effect of baffles on the mentioned distance occurred for Fr = 2.00, 1.30, and 0.82. Compared to the un-baffled weir, these distances were 8.8, 15, and 19% farther at the relative drop heights of 1.72, 0.78, and 0.31, respectively. This suggests that the presence of baffles can significantly reduce the maximum scour depth and extend the distance of the scour hole, particularly under moderate to high Froude number conditions and varying relative drop heights. The baffles appear to effectively dissipate the flow energy and disrupt the sediment transport processes, leading to a less pronounced scour profile. Interestingly, it was also observed that the length of the scour hole for the baffled and un-baffled weirs, with Fr = 0.76 and $\Delta H/h_d$ = 0.27, which is lower than the weir height. However, for other flow conditions, the scour hole length is greater than the weir height. This highlights the complex interplay between the hydraulic parameters and the resulting bed morphology, which should be carefully considered in the design and operation of such structures.

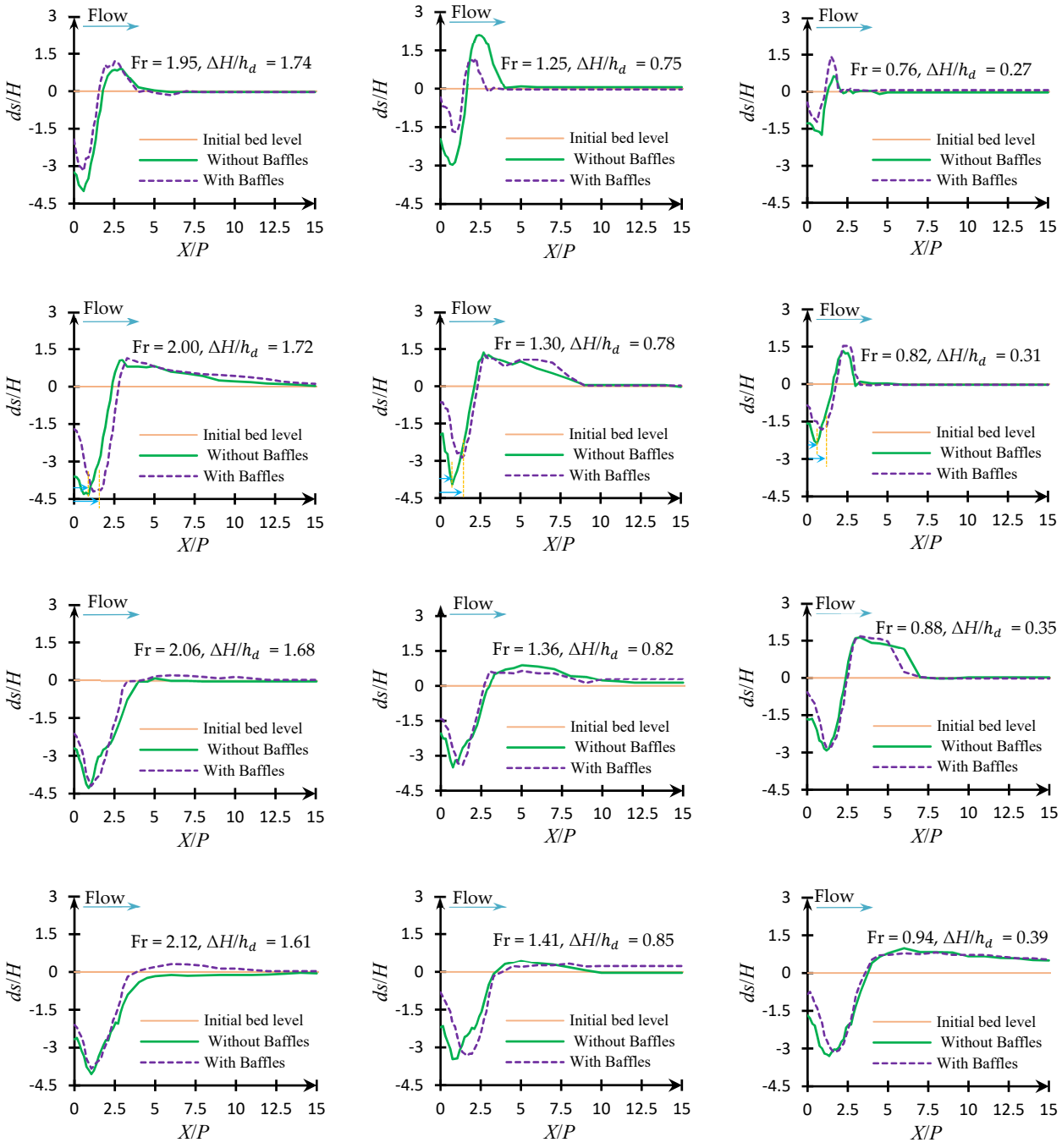

(**a**) $1.61 \leq \Delta H/h_d \leq 1.74$ (**b**) $0.75 \leq \Delta H/h_d \leq 0.85$ (**c**) $0.27 \leq \Delta H/h_d \leq 0.39$

Figure 15. Comparison of the longitudinal bed profiles downstream of the weirs with and without baffles.

Equation (2) describes the relationship between the relative maximum scour depth and the relative weir toe scour as a function of the Froude number and the relative drop height, as shown in Figure 16. The results indicate that the relative maximum scour depth and weir toe scour increase with higher Froude numbers for both baffled and un-baffled weirs. Importantly, the presence of baffles significantly reduces weir toe scour by altering the downstream flow. At constant Froude numbers, baffled weirs exhibit lower relative maximum scour depth and weir toe scour compared to un-baffled weirs. Specifically, the

TPKW shows 9.7 and 14% reductions in maximum scour depth and weir toe scour, respectively, compared to the RPKW. The effectiveness of baffles in reducing scour is more pronounced when the tailwater depth is lower, as the baffles can influence a greater portion of the flow layers in this scenario. However, baffles still significantly mitigate weir toe scour, even when the tailwater depth is high, by transforming the impinging jets into surface jets. This change in flow pattern improves the overall stability of the weir structure.

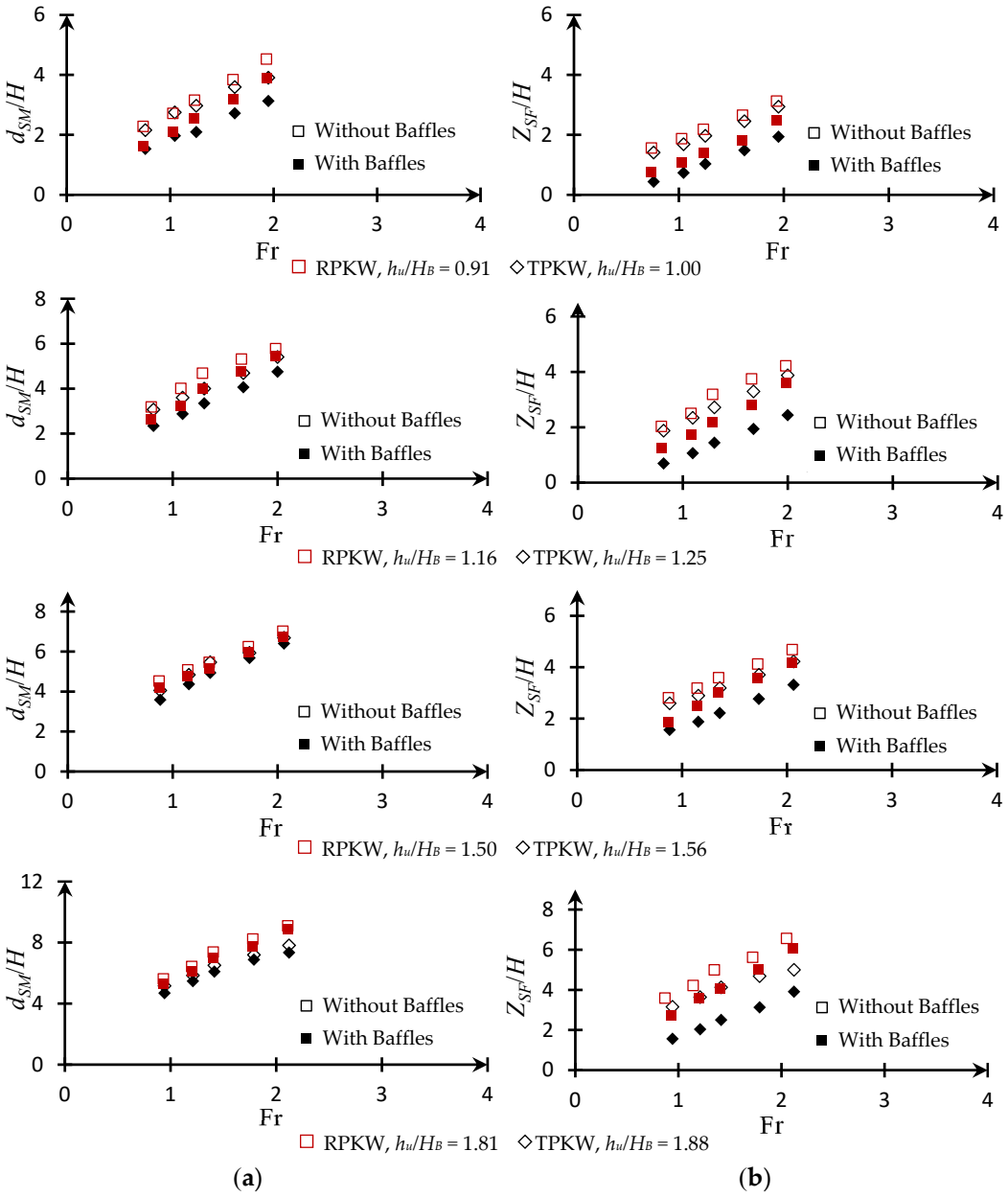

Figure 16. Changes of: (**a**) relative maximum scour depth, and (**b**) relative weir toe scour depth with Froude number.

The percentage scour reduction for the maximum scour depth, weir toe scour depth, maximum scour depth location, and scour hole length, for different tests, are presented in Figure 17.

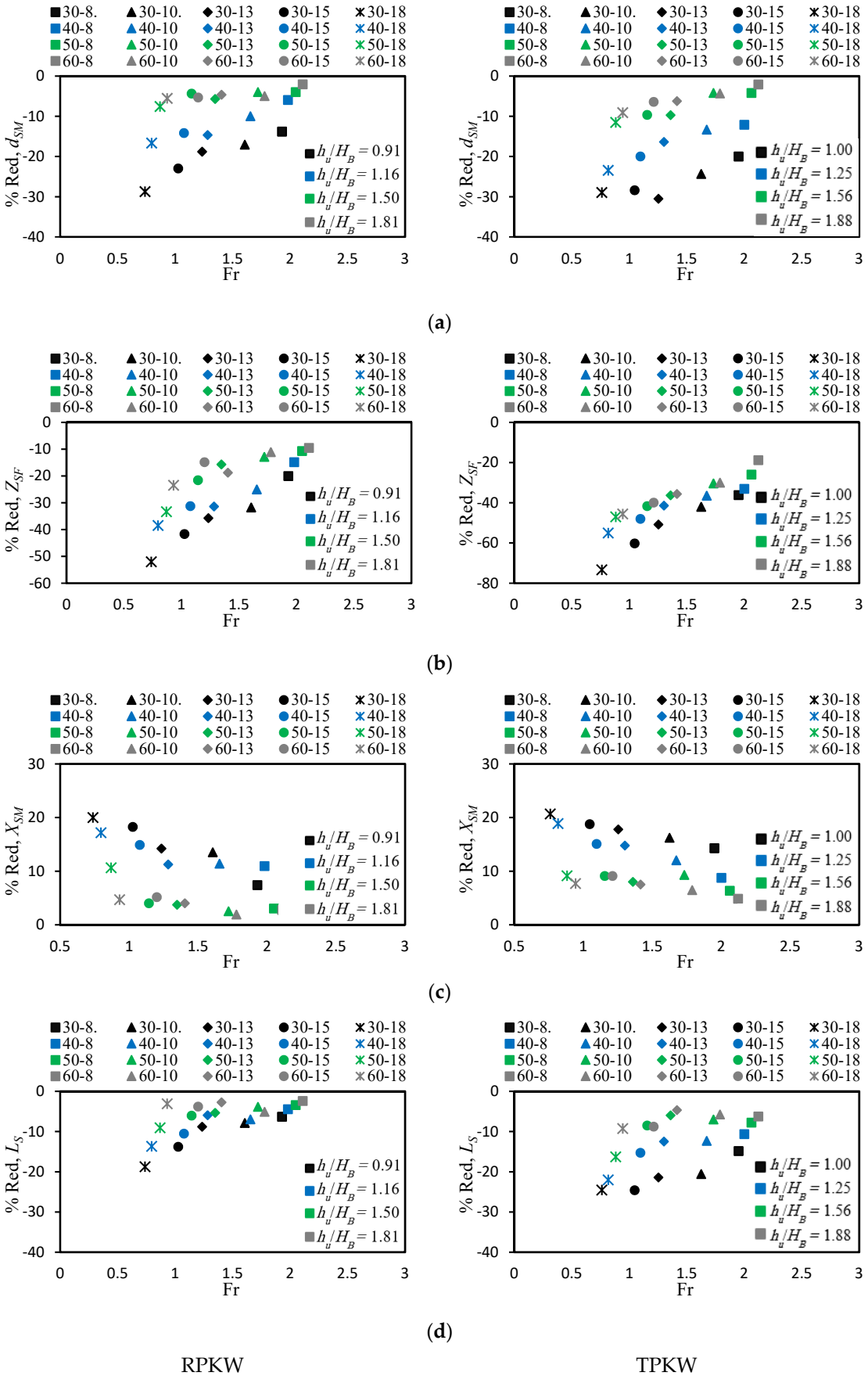

Figure 17. Percentage reduction in (**a**) d_{SM}, (**b**) Z_{SF}, (**c**) X_{SM} and (**d**) L_S with and without baffles.

According to Figure 17, baffled weirs show significant reductions in maximum scour depth (11–14%) in RPKW and TPKW [Figure 17a] and weir toe scour (25–41%) in RPKW and TPKW compared to un-baffled weirs [Figure 17b]. The effect is more pronounced at lower Froude numbers when more flow layers are affected by the baffles. Furthermore, baffled weirs experience a 9–11.7% downstream shift in the location of maximum scour depth [Figure 17c] and a 7–13% reduction in scour hole length [Figure 17d]. The greatest reduction (25%) in scour hole length was observed in the TPKW with test B30-18.

The scour hole areas and volumes were calculated using Tecplot 360 EX software and presented in Table 6. The presence of baffles had a significant impact on reducing scour. The greatest effects were observed in test B30-18, where baffles reduced the scour hole area and volume by 58.2 and 61.8%, respectively, compared to un-baffled TPKWs. In general, baffles are more effective at reducing scour downstream of TPKWs compared to RPKWs. This is due to the influence of the weir keys in TPKWs, which allows the baffles to achieve greater reductions in scour hole size. In contrast, baffles have a less dramatic impact on mitigating downstream scour around RPKWs. On average, baffles reduced the scour hole area and volume by 31.6 and 32.2% in TPKWs, respectively, compared to 26.7 and 30.3% in RPKWs. This suggests that the presence of baffles is more effective in mitigating scour in TPKWs under the tested hydraulic conditions.

Table 6. Comparison of area and volume of scour hole downstream of weirs with and without baffles.

Symbol of Test	Difference (%)		Difference (%)	
	A_S		V_S	
#	**RPKW**	**TPKW**	**RPKW**	**TPKW**
30-8	35.5	38	36.5	39
30-10	31	35	44.4	45.7
30-13	25.8	31.8	51.2	52.3
30-15	42.3	45.3	56.8	57.2
30-18	56.2	**58.2**	60.9	**61.8**
40-8	27.3	37.3	19.3	21
40-10	26.5	35	31.5	34
40-13	29	31	44.1	46.8
40-15	21.2	24.2	40	41
40-18	16.6	17.1	33.3	34.2
50-8	34.8	39.8	25.3	26.9
50-10	27	34.5	32.5	34
50-13	23	29	20	20.5
50-15	15.5	18	24	25
50-18	5.6	6.1	29.4	31.4
60-8	14.3	19.3	20.6	26.2
60-10	27	34	15.5	19
60-13	36.8	47.8	8.5	11.8
60-15	25	32.5	7.25	9.65
60-18	13.3	18.3	4.9	6.9
Average (%)	26.7	31.6	30.3	32.2

This research developed empirical equations to accurately predict the relative scour depths (d_{SM}/H and Z_{SF}/H) downstream of a weir, applicable for scenarios both without baffles (Equation (8)) and with baffles (Equation (9)). These equations can effectively calculate the scour parameters for both RPKWs and TPKWs. The equations accommodate a wide range of hydraulic conditions, including $0.74 \le Fr \le 2.12$, $0.26 \le \Delta H/h_d \le 1.74$, and $0.99 \le h_u/H_B \le 1.88$.

$$\frac{\psi}{H} = K_{\zeta}\,(\mathrm{Fr})^{a}\left(\frac{\Delta H}{h_d}\right)^{b} \tag{8}$$

$$\frac{\psi}{H} = K_{\zeta}\,(\mathrm{Fr})^{a}\left(\frac{\Delta H}{h_d}\right)^{b}\left(\frac{h_u}{H_B}\right)^{c} \tag{9}$$

The coefficient K_{ζ} accounts for the influence of weir shape, and Table 7 outlines the empirical constants 'a', 'b', and 'c'. This table also includes the coefficient of determination R^2, RMSE, and MRPE to comprehensively assess the precision and accuracy of the developed equations. According to Table 7, these equations estimate scour parameters, achieving impressive results with an average R^2 = 0.951, RMSE = 0.145, and MRPE = 4.429%. Figure 18 compares calculated and observed scour depths for weirs with and without baffles. This visual comparison demonstrates the high accuracy and predictive capability of the proposed equations, which can reliably estimate the scour depths under a wide range of hydraulic conditions.

Table 7. Coefficients, exponents, and statistical indices of Equations (8) and (9).

Ψ	Eq. N	Weir	K_{ζ}	*a*	*b*	#	c	R^2	RMSE	MRPE (%)
d_{SM}	8	RPKW	3.327	0.488	0.048	un-baffled	-	0.954	0.175	3.857
		TPKW	2.845					0.961	0.119	2.856
	9	RPKW	2.737	0.734	0.013	baffled	0.408	0.925	0.227	6.081
		TPKW	1.945					0.951	0.167	4.141
Z_{SF}	8	RPKW	2.755	0.063	0.355	un-baffled	-	0.945	0.140	3.641
		TPKW	2.234					0.955	0.101	3.472
	9	RPKW	2.215	0.014	0.565	baffled	0.248	0.945	0.154	6.263
		TPKW	1.340					0.971	0.076	5.120

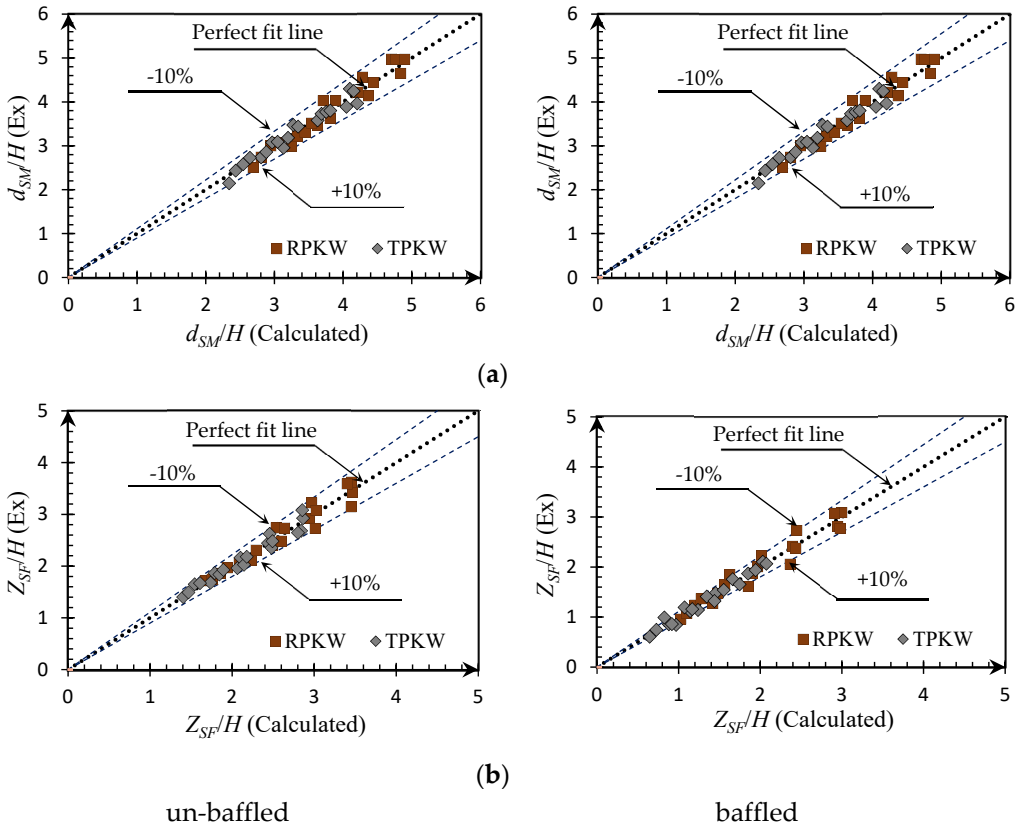

Figure 18. Comparison of the observed and calculated values of: (**a**) maximum scour depth and (**b**) weir toe scour depth.

3.2. Modeling Outputs

This study evaluated the performance of optimized MLP, SVR, and XGBoost models in predicting maximum scour depth and weir toe scour depth, both with and without baffles, for training and testing datasets. Table 8 demonstrates that the MLP model outperforms both XGBoost and SVR in predicting d_{SM}/H across all scenarios, with superior performance in both the training and testing phases. The MLP model achieves an averaged R^2 of 0.988, RMSE of 0.035, and MRPE of 1.036% across all scenarios. The adoption of the MLP model over XGBoost and SVR yields substantial improvements, with notable increases in R^2 (4.50% and 0.2%), decreases in RMSE indices (5.8% and 0.5%), and significant reductions in MRPE indices (135.8% and 13.3%).

Specifically, the MLP model achieves superior results for maximum scour depth prediction. It outperforms both un-baffled and baffled RPKW scenarios by 3.7% and 6.7% in terms of R^2 and surpasses un-baffled and baffled TPKW scenarios by 2% and 4%. The MLP model yields RMSE values of 0.046 for un-baffled RPKW and 0.035 for baffled RPKW, which are better than the results in Table 7 (0.175 and 0.227, respectively). In un-baffled and baffled TPKW scenarios, the MLP model's RMSE values are 0.036 and 0.024, outperforming the corresponding values from Equations (8) and (9) (0.119 and 0.167). Regarding MRPE, the MLP model significantly outperforms Equations (8) and (9) for both RPKW and TPKW scenarios.

Table 8. The results of d_{SM}/H and statistical indices.

Weir Type	Model	R^2 Train	R^2 Test	RMSE Train	RMSE Test	MRPE Train	MRPE Test
RPKW, (un-baffled)	XGBoost	0.828	0.944	0.334	0.104	7.753	2.602
	SVR	0.948	0.987	0.183	0.051	4.290	1.377
	MLP	0.944	**0.989**	0.190	**0.046**	4.713	**1.244**
RPKW, (Baffled)	XGBoost	0.924	0.967	0.248	0.055	6.331	1.578
	SVR	0.969	0.883	0.159	0.103	4.027	2.565
	MLP	0.966	**0.987**	0.167	**0.035**	3.973	**0.992**
TPKW, (un-baffled)	XGBoost	0.855	0.959	0.242	0.066	5.328	1.527
	SVR	0.999	0.924	0.010	0.090	0.315	2.700
	MLP	0.942	**0.988**	0.153	**0.036**	4.283	**1.138**
TPKW, (Baffled)	XGBoost	0.988	0.938	0.083	0.057	2.380	1.879
	SVR	0.982	0.846	0.103	0.090	2.947	3.183
	MLP	0.981	**0.989**	0.006	**0.024**	0.184	**0.769**

The performance of the different ML models in predicting Z_{SF}/H for various scenarios is summarized in Table 9. For un-baffled RPKW, the MLP model outperformed XGBoost and SVR, achieving the highest R^2 (0.998), lowest RMSE (0.004), and lowest MRPE (0.167). For baffled RPKW, the MLP model again demonstrated superior performance. For un-baffled TPKW, the MLP model had the highest R^2 (0.992), lowest RMSE (0.024), and lowest MRPE (0.904). However, for baffled TPKW, XGBoost performed best, with the highest R^2 (0.965), lowest RMSE (0.048), and lowest MRPE (2.798).

The MLP consistently outperformed XGBoost and SVR models across most configurations, except for baffled TPKW, where XGBoost performed better. The significant improvements in statistical indices demonstrate the MLP model's robustness and accuracy in predicting Z_{SF}/H, outperforming traditional models. Specifically, the MLP model surpasses both un-baffled and baffled RPKW scenarios by 97% and 87% in terms of RMSE and outperforms un-baffled and baffled TPKW scenarios by 76% and 33%.

Table 9. The results of Z_{SF}/H and statistical characteristics.

Weir Type	Model	R^2 Train	R^2 Test	RMSE Train	RMSE Test	MRPE Train	MRPE Test
RPKW, (un-baffled)	XGBoost	0.881	0.918	0.215	0.102	7.146	4.325
	SVR	0.925	0.995	0.170	0.024	4.443	0.900
	MLP	0.933	**0.998**	0.161	**0.004**	4.222	**0.167**
RPKW, (Baffled)	XGBoost	0.999	0.962	0.009	0.054	0.439	2.330
	SVR	0.976	0.907	0.106	0.085	3.475	4.517
	MLP	0.998	**0.994**	0.011	**0.020**	0.422	**1.084**
TPKW, (un-baffled)	XGBoost	0.68	0.868	0.277	0.103	11.216	4.557
	SVR	0.959	0.937	0.100	0.071	3.729	3.516
	MLP	0.937	**0.992**	0.123	**0.024**	4.572	**0.904**
TPKW, (Baffled)	XGBoost	0.949	**0.965**	0.103	**0.048**	7.023	**2.798**
	SVR	0.976	0.849	0.069	0.100	4.405	9.680
	MLP	0.997	0.960	0.003	0.051	0.230	4.794

Table 10 illustrates the feature importance analysis conducted by the MLP model. This analysis sheds light on the relative significance of each input variable in determining the model's predictive accuracy. According to the results depicted in Table 10, it is evident that in the scenario without baffles, the impact of $\Delta H/h_d$ on d_{SM}/H and Z_{SF}/H outweighs that on Fr, except in the case of Z_{SF}/H for the un-baffled RPKW, where the influence of Fr exceeds $\Delta H/h_d$ by 46%. On the other hand, for the baffled PKW, hu/H_B emerges as the most crucial parameter in predicting d_{SM}/H and Z_{SF}/H. The importance scores reflect this, with values of 0.493 and 0.672 for predicting d_{SM}/H in RPKW and TPKW, and 0.403 and 0.355 for predicting Z_{SF}/H in RPKW and TPKW, respectively.

Table 10. Feature importance analysis by the MLP model.

Features	Weir Model	Importance Score		
		Fr	$\Delta H/h_d$	h_u/H_B
d_{SM}/H	RPKW (un-baffled)	0.418	**0.582**	-
	RPKW (baffled)	0.240	0.267	**0.493**
	TPKW (un-baffled)	0.431	**0.569**	-
	TPKW (baffled)	0.164	0.164	**0.672**
Z_{SF}/H	RPKW (un-baffled)	**0.593**	0.407	-
	RPKW (baffled)	0.260	0.340	**0.403**
	TPKW (un-baffled)	0.484	**0.516**	-
	TPKW (baffled)	0.327	0.318	**0.355**

Figure 19 presents a comparison of the estimated values of d_{SM}/H and Z_{SF}/H using XGBoost, MLP, and SVR models against their measured values. The majority of the forecasted test data fall within ±10% error lines, confirming that the proposed machine learning models accurately predict scour parameters for PKWs. The results show that the MLP model consistently outperforms the other models.

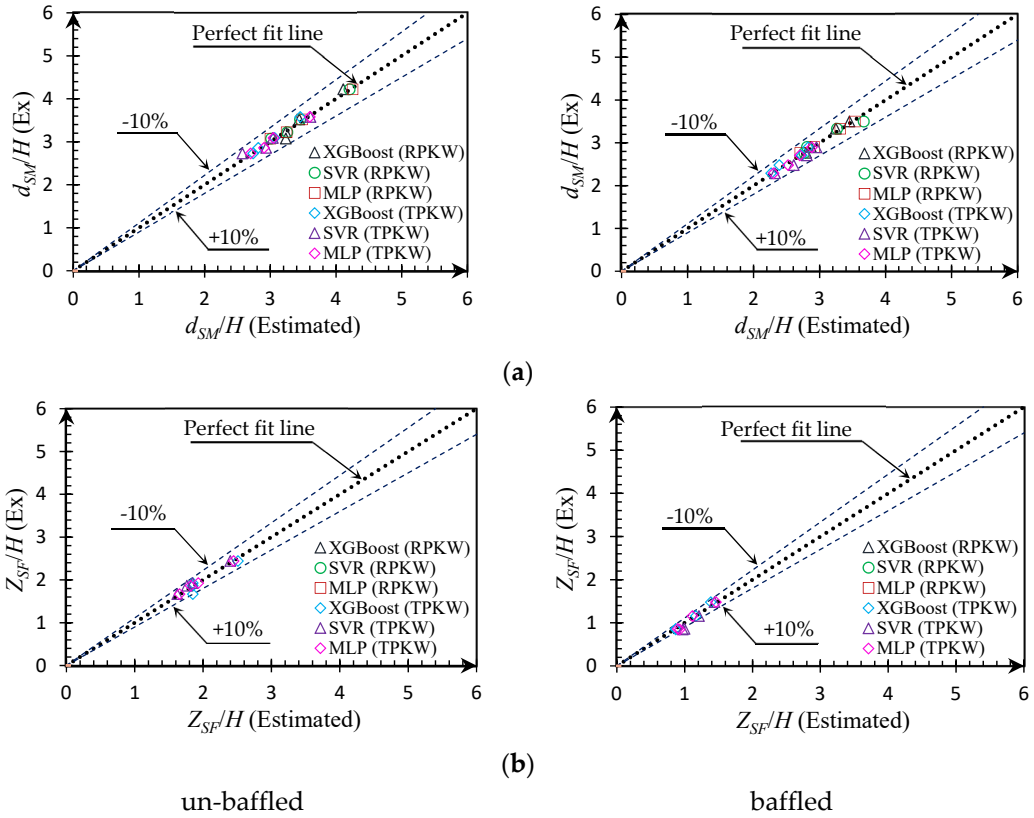

Figure 19. Comparison of machine learning models for predicting of: (**a**) maximum scour depth and (**b**) weir toe scour depth.

The Taylor plots (Figure 20) compare the performance of ML models in predicting d_{SM}/H and Z_{SF}/H for baffled and un-baffled RPKW and TPKW. The MLP model consistently demonstrates superior performance, with the highest correlation and closest alignment with measured data, indicating superior predictive performance and alignment with actual measurements. XGBoost and SVR models also perform well but with slightly lower correlation and higher deviation compared to the MLP model.

Additionally, the Taylor plots provide a visual representation of the models' standard deviation and correlation coefficient relative to the observed data. The closer a model's point is to the reference point, the better its performance in terms of matching the observed variability and correlation. The MLP model's points are closest to the reference point for both d_{SM}/H and Z_{SF}/H predictions, further confirming its superior performance compared to the other models.

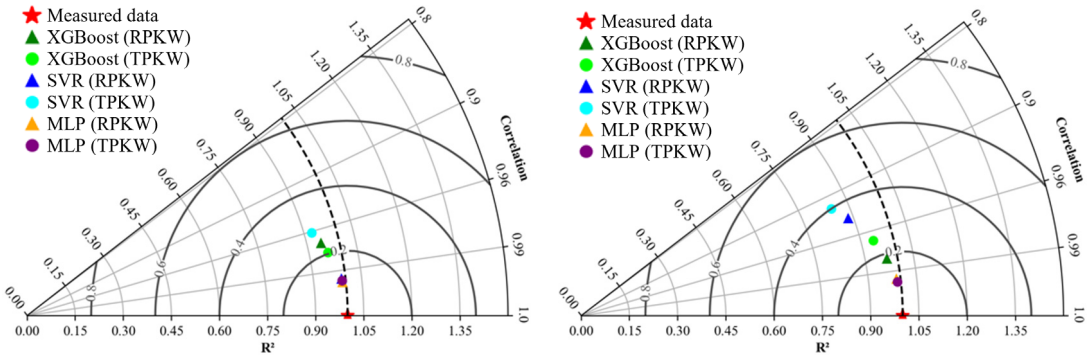

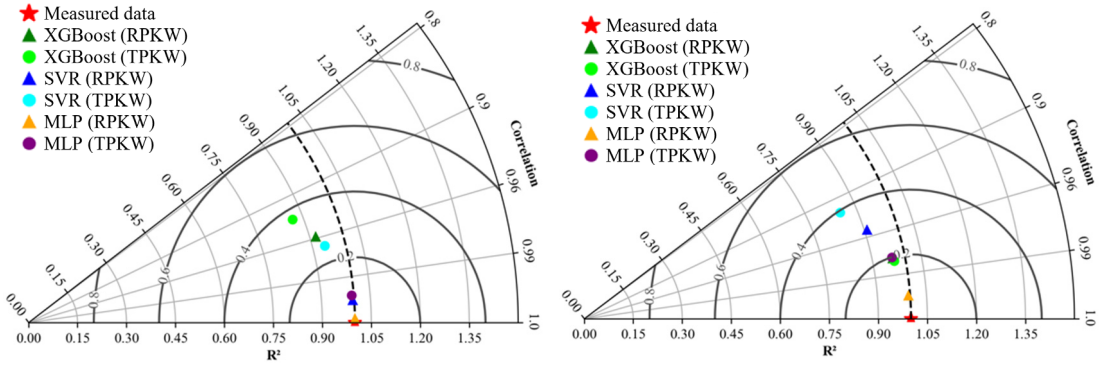

(**b**)

un-baffled baffled

Figure 20. Taylor diagrams for predictions of: (**a**) maximum scour depth and (**b**) weir toe scour depth.

4. Conclusions

This comprehensive study has investigated the effects of baffled outlet keys on energy dissipation and bed topographical changes downstream of rectangular piano key weirs (RPKWs) and trapezoidal piano key weirs (TPKWs) under various hydraulic conditions. Advanced machine learning models, including MLP, SVR, and XGBoost, have also been implemented to predict scour depths accurately. The key findings and applications of this work are as follows:

1. The presence of baffles in weir outlet keys significantly alters the flow patterns, changing from impinging jets in un-baffled weirs to surface jets in baffled weirs. This effect leads to increased energy losses, with the average energy loss in RPKW and TPKW with baffles being 22% and 18% higher, respectively, compared to the weir without baffles. This effect is more pronounced at lower Froude numbers, when the baffles affect more flow layers. Baffles have a more significant reducing effect at lower relative drop heights. Conversely, increasing the Froude number and relative drop height increases scour depth.
2. The baffles significantly reduce scour depths and their temporal variations, with baffled RPKW and TPKW weirs showing, on average, an 11% and 14% reduction in scour depth at equilibrium compared to un-baffled weirs.
3. The baffles significantly reduce topographical changes and scour hole extension, resulting in a downstream shift of 9% and 11.7% in the maximum scour depth location for RPKW and TPKW, respectively, and reductions of 7% and 13% in scour hole length for RPKW and TPKW, respectively. Additionally, the relative maximum scour depth and weir toe scour increase with higher Froude numbers for both baffled and un-baffled weirs.
4. Baffles reduced the scour hole area and volume by 26.7% and 30.3% in RPKWs and 31.6% and 32.2% in TPKWs. The effects of baffles on reducing scouring were more significant in TPKWs than RPKWs and more pronounced at lower Froude numbers. This information can be utilized to design more stable and resilient hydraulic structures, mitigating the risk of foundation erosion and ensuring the long-term integrity of critical infrastructure.
5. Novel empirical equations were introduced to accurately predict the relative scour depths downstream of a PKW, applicable for scenarios both without baffles (Equation (8)) and with baffles (Equation (9)), achieving impressive results with an average $R^2 = 0.951$, RMSE = 0.145, and MRPE = 4.429%.
6. The study has demonstrated the superior performance of the MLP machine learning model in estimating local scour characteristics downstream of PKWs. It outperformed traditional regression models (Equations (8) and (9)) and other machine

learning algorithms in most scenarios with an average R^2 = 0.988, RMSE = 0.035, and MRPE = 1.036%, except in predicting weir toe scour depth for baffled TPKW, where XGBoost performed better with R^2 = 0.965, RMSE = 0.048, and MRPE = 2.798%. This predictive tool can be integrated into the design process, enabling engineers to accurately assess scour risks and optimize the structural design of weirs and similar hydraulic structures.

7. Taylor plots confirmed the MLP model's robustness, with high correlation and low prediction error. In conclusion, the optimized MLP model offers a robust and reliable predictive tool for assessing scour characteristics in PKW designs within the specified range of $0.74 \leq Fr \leq 2.12$, $0.26 \leq \Delta H/h_d \leq 1.74$, and $0.99 \leq h_u/H_B \leq 1.88$, outperforming traditional empirical approaches and other ML models in most evaluated scenarios.
8. The feature importance analysis by the MLP model provides insights into the relative contribution of each input variable. For un-baffled PKW, $\Delta H/h_d$ effect on scour is greater than Fr, except for RPKW weir toe scour where Fr effect is 46% more. For baffled PKW, h_u/H_B is most important in forecasting scour.
9. The findings from this study contribute to a deeper understanding of the intricate relationships between flow patterns, energy dissipation, and bed topography in the context of PKWs. These insights can be leveraged to enhance the design and performance of PKWs, resulting in more efficient, sustainable, and resilient structures.

Author Contributions: Conceptualization, C.A.C. and M.G.; methodology, C.A.C., A.F. and M.G.; validation, C.A.C. and E.K.; formal analysis, C.A.C. and M.G.; investigation, C.A.C., M.G. and M.L.; resources, C.A.C. and M.G.; data curation, C.A.C. and M.G.; writing—original draft preparation, C.A.C. and E.K.; writing—review and editing, M.G. and M.L.; visualization, C.A.C. and M.G.; supervision, M.G. All authors have read and agreed to the published version of the manuscript.

Funding: This research received no external funding.

Data Availability Statement: Some or all of the data, models, or code that support the findings of this study are available from the first author upon reasonable request.

Acknowledgments: The authors would like to express their sincere gratitude to the University of Exeter for covering the APC and to Modares Science and Technology Park for their partial financial support of this project.

Conflicts of Interest: The authors declare no conflicts of interest.

References

1. Pilarczyk, K.W.; Jo, Y.C.; Yun, O. Stability of rock-fill structures. *Mag. Korean Soc. Agric. Eng.* **1991**, *33*, 17–40.
2. Jüstrich, S.; Pfister, M.; Schleiss, A.J. Mobile riverbed scours downstream of a Piano key weir. *J. Hydraul. Eng.* **2016**, *142*, 04016043. https://doi.org/10.1061/(ASCE)HY.1943-7900.0001189.
3. Palermo, M.; Crookston, B.; Pagliara, S. Analysis of equilibrium morphologies downstream of a PK weir structure. In *World Environmental and Water Resources Congress 2020: Hydraulics, Waterways, and Water Distribution Systems Analysis*; American Society of Civil Engineers: Reston, VA, USA, 2020; pp. 43–51. https://doi.org/10.1061/9780784482971.005.
4. Kumar, B.; Ahmad, Z. Experimental study on scour downstream of a Piano key weir with nose. In Proceedings of the 8th IAHR ISHS, Santiago, Chile, 12–15 May 2020. https://doi.org/10.14264/uql.2020.595.
5. Kumar, B.; Kadia, S.; Ahmad, Z. Sediment movement over type A Piano key weir. *J. Irrig. Drain. Eng.* **2021**, *147*, 04021018. https://doi.org/10.1061/(ASCE)IR.1943-4774.0001561.
6. Ghodsian, M.; Abdi Chooplou, C.; Ghafouri, A. Scouring downstream of triangular and trapezoidal Piano key weirs. *J. Hydraul.* **2021**, *16*, 43–58. https://doi.org/10.30482/jhyd.2021.261439.1497.
7. Lantz, W.; Crookston, B.M.; Palermo, M. Apron and cutoff wall scour protection for Piano key weirs. *Water* **2021**, *13*, 2332. https://doi.org/10.3390/w13172332.
8. Kumar, B.; Ahmad, Z. Scour downstream of a Piano key weir with and without a solid apron. *J. Irrig. Drain. Eng.* **2022**, *148*, 04021066. https://doi.org/10.1061/(ASCE)IR.1943-4774.0001647.
9. Abdi Chooplou, C.; Bodaghi, E.; Ghodsian, M.; Vaghefi, M. Temporal evolution of scouring downstream of a trapezoidal Piano key weir. *Int. J. River Basin Manag.* **2022**, 1–14. https://doi.org/10.1080/15715124.2022.2143513.
10. Lantz, W.D.; Crookston, B.M.; Palermo, M. Evolution of local scour downstream of type A PK weir in non-cohesive sediments. *J. Hydrol. Hydromech.* **2022**, *70*, 103–113. https://doi.org/10.2478/johh-2021-0035.

11. Abdi Chooplou, C.; Kazerooni, S.; Ghodsian, M.; Vaghefi, M. Experimental study of scouring downstream of type-A Piano key weirs. *Arab. J. Geosci.* **2022**, *15*, 1702. https://doi.org/10.1007/s12517-022-11001-9.
12. Abdi Chooplou, C.; Ghodsian, M.; Davoud, A.; Ghafouri, A. An experimental and numerical study on the flow field and scour downstream of rectangular piano key weirs with crest indentations. *Innov. Infrastruct. Solut.* **2023**. *8*, 140. https://doi.org/10.1007/s41062-023-01108-7.
13. Bodaghi, E.; Abdi Chooplou, C.; Ghodsian, M. Experimental investigation of scour downstream of a type A trapezoidal piano key weir under free and submerged flow conditions. *J. Hydrol. Hydromech.* **2024**, *72*, 34–48. https://doi.org/10.2478/johh-2023-0041.
14. Abdi Chooplou, C.; Ghodsian, M.; Ghafouri, A. Local scour downstream of various shapes of piano key weirs. *Innov. Infrastruct. Solut.* **2024**, *9*, 117. https://doi.org/10.1007/s41062-024-01411-x.
15. Fathi, A.; Abdi Chooplou, C.; Ghodsian, M. Local scour downstream of type-A trapezoidal stepped piano key weir in sand and gravel sediments. *ISH J. Hydraul. Eng.* **2024**, 1–13. https://doi.org/10.1080/09715010.2024.2353612.
16. Kumar, B.; Pandey, M.; Ahmad, Z. Flow field and sediment passing capacity of type-a piano key weirs. *Int. J. Sediment Res.* **2024**. https://doi.org/10.1016/j.ijsrc.2024.04.005.
17. Erpicum, S.; Machiels, O. Energy dissipation on a stepped spillway downstream of a Piano key weir—experimental study. In Proceedings of the International Conference on Labyrinth Piano Key Weirs, Taylor & Francis Group, London, UK, 9–11 February 2011.
18. Eslinger, K.R.; Crookston, B.M. Energy dissipation of type A Piano key weir. *Water* **2020**, *12*, 1253. https://doi.org/10.3390/w12051253.
19. Naghibzadeh, S.M.; Heidarnezhad, M.; Masjedi, A.; Bordbar, A. Experimental and numerical analysis of energy dissipation in Piano key weirs with stepped and baffled barriers at downstream slope. *Iran. J. Soil Water Res.* **2020**, *51*, 2431–2442. https://doi.org/10.22059/ijswr.2020.295541.668467.
20. Souri, J.; OmidvarMohammadi, H.; Salehi Neyshabouri, S.A.A.; Abdi Chooplou, C.; Kahrizi, E.; Akbari, H. Numerical simulation of aeration impact on the performance of a-type rectangular and trapezoidal piano key weirs. *Model. Earth Syst. Environ.* **2024,** 1–20. https://doi.org/10.1007/s40808-024-02058-4.
21. Iqbal, M.; Ghani, U. Effect of variation in key slope ratios and key width ratios on energy dissipation over a piano key weir. *Iran. J. Sci. Technol. Trans. C* **2024**, *48*, 2725–2739. https://doi.org/10.1007/s40996-023-01312-6.
22. Muzzammil, M. ANFIS approach to the scour depth prediction at a bridge abutment. *J. Hydroinf.* **2010**, *12*, 474–485. https://doi.org/10.2166/hydro.2010.004.
23. Najafzadeh, M.; Barani, G.A.; Kermani, M.R.H. Abutment scour in clear-water and live-bed conditions by GMDH network. *Water Sci. Technol.* **2013**, *67*, 1121–1128. https://doi.org/10.2166/wst.2013.670.
24. Etemad-Shahidi, A.; Bonakdar, L.; Jeng, D.S. Estimation of scour depth around circular piers: Applications of model tree. *J. Hydroinf.* **2015**, *17*, 226–238. https://doi.org/10.2166/hydro.2014.151.
25. Sharafi, H.; Ebtehaj, I.; Bonakdari, H.; Zaji, A.H. Design of a support vector machine with different kernel functions to predict scour depth around bridge piers. *Nat. Hazard.* **2016**, *84*, 2145–2162.
26. Azimi, H.; Bonakdari, H.; Ebtehaj, I.; Talesh, S.H.A.; Michelson, D.G.; Jamali, A. Evolutionary Pareto optimization of an ANFIS network for modeling scour at pile groups in clear water condition. *Fuzzy Sets Syst.* **2017**, *319*, 50–69. https://doi.org/10.1016/j.fss.2016.10.010.
27. Ebtehaj, I.; Bonakdari, H.; Moradi, F.; Gharabaghi, B.; Khozani, Z.S. An integrated framework of extreme learning machines for predicting scour at pile groups in clear water condition. *Coast. Eng.* **2018**, *135*, 1–15. https://doi.org/10.1016/j.coastaleng.2017.12.012.
28. Rashki Ghaleh Nou, M.; Azhdary Moghaddam, M.; Shafai Bajestan, M.; Azamathulla, H.M. Estimation of scour depth around submerged weirs using self-adaptive extreme learning machine. *J. Hydroinf.* **2019**, *21*, 1082–1101. https://doi.org/10.2166/hydro.2019.070.
29. Sharafati, A.; Haghbin, M.; Haji Seyed Asadollah, S.B.; Tiwari, N.K.; Al-Ansari, N.; Yaseen, Z.M. Scouring depth assessment downstream of weirs using hybrid intelligence models. *Appl. Sci.* **2020**, *10*, 3714. https://doi.org/10.3390/app10113714.
30. Salih, S.Q.; Habib, M.; Aljarah, I.; Faris, H.; Yaseen, Z.M. An evolutionary optimized artificial intelligence model for modeling scouring depth of submerged weir. *Eng. Appl. Artif. Intell.* **2020**, *96*, 104012. https://doi.org/10.1016/j.engappai.2020.10401.
31. Ahmadianfar, I.; Jamei, M.; Karbasi, M.; Sharafati, A.; Gharabaghi, B. A novel boosting ensemble committee-based model for local scour depth around non-uniformly spaced pile groups. *Eng. Comput.* **2021**, *38*, 3439–3461. https://doi.org/10.1007/s00366-021-01370-2.
32. Pandey, M.; Karbasi, M.; Jamei, M.; Malik, A.; Pu, J.H. A comprehensive experimental and computational investigation on estimation of scour depth at bridge abutment: Emerging ensemble intelligent systems. *Water Resour. Manag.* **2023**, *37*, 3745–3767.
33. Salmasi, F.; Sihag, P.; Abraham, J.; Nouri, M. Experimental investigation and prediction of free fall jet scouring using machine learning models. *Int. J. Sediment Res.* **2023**, *38*, 405–420. https://doi.org/10.1016/j.ijsrc.2022.11.004.
34. Iqbal, M.; Ghani, U. Prediction of the discharge capacity of piano key weirs using artificial neural networks. *J. Hydroinformatics* **2024**, *26*, 1167–1188. https://doi.org/10.2166/hydro.2024.303.
35. Ettema, R. *Hydraulic Modeling: Concepts and Practice*; ASCE: Reston, VA, USA, 2000; p. 97.

36. Haghnazar, H.; Saneie, M. Impacts of pit distance and location on river sand mining management. *Model. Earth Syst. Environ.* **2019**, *5*, 1463–1472. https://doi.org/10.1007/s40808-019-00627-6.
37. Pfister, M.; Battisacco, E.; De Cesare, G.; Schleiss, A.J. Scale effects related to the rating curve of cylindrically crested Piano key weirs. In *Labyrinth Piano Key Weirs II*; CRC/Balkema: Leiden, Netherlands, 2013; pp. 73–82.
38. Erpicum, S.; Tullis, B.P.; Lodomez, M.; Archambeau, P.; Dewals, B.J.; Pirotton, M. Scale effects in physical Piano key weirs models. *J. Hydraul. Res.* **2016**, *54*, 692–698. https://doi.org/10.1080/00221686.2016.1178577.
39. Novak, P.; Cabelka, J. Monographs & surveys in water resources engineering. In *Models in Hydraulic Engineering: Physical Principles and Design Applications*, 4th ed.; Pitman Publishing: Boston, MA, USA, 1981; pp. 1–459.
40. Lempérière, F.; Ouamane, A. The Piano key weir: A new cost-effective solution for spillways. *Int. J. Hydropower Dams* **2003**, *10*, 144–149.
41. Lempérière, F.; Jun, G. Low cost increase of dams storage and flood mitigation: The Piano key weir. In Proceedings of the 19th Congress of ICID, Beijing, China, 18 September 2005.
42. Mehboudi, A.; Attari, J.; Hosseini, S.A. Experimental study of discharge coefficient for trapezoidal PKWs. *Flow Meas. Instrum.* **2016**, *50*, 65–72. https://doi.org/10.1016/j.flowmeasinst.2016.06.005.
43. Chiew, Y.M. Local Scour at Bridge Piers. Rep. No. 355. Ph.D. thesis, Department of Civil Engineering, University of Auckland, Auckland, New Zealand, 1984.
44. Chiew, Y.M.; Melville, B. Local scour at bridge piers with non-uniform sediments. *Proc. Inst. Civ. Eng. Water Eng. Group* **1989**, *87*, 215–224.
45. Ho Ta Khanh, M.; Quat, D.S.; Thuy, D.X. Piano key weirs under design and construction in Vietnam. In *Labyrinth and Piano Key Weirs*; CRC/Balkema: Leiden, Netherlands, 2011; pp. 225–232.
46. Laugier, F.; Vermeulen, J.; Lefebvre, V. Overview of PKWs experience developed at EDF during the past few years. In *Labyrinth and PKWs II*; CRC: Boca Raton, FL, USA, 2013; pp. 213–226. https://doi.org/10.1201/B15985-30
47. Pagliara, S.; Hager, W.H.; Minor, H.E. Hydraulics of plane plunge pool scour. *J. Hydraul. Eng.* **2006**, *132*, 450–461. https://doi.org/10.1061/(ASCE)0733-9429132:5(450).
48. United States Bureau of Reclamation. *Design of Small Dams*, 3th ed.; US Department of the Interior, Bureau of Reclamation: Washington, DC, USA, 1987.
49. Dugué, V.; Pfister, M.; Hachem, F.; Boillat, J.L.; Nagel, V.; Laugier, F. Étude sur modèle physique du nouvel évacuateur de crue du barrage de Gage II. *La Houille Blanche* **2013**, *2*, 31–38. https://doi.org/10.1051/lhb/2013013.
50. Chiew, Y.M. Scour protection at bridge piers. *J. Hydraul. Eng.* **1992**. *118*, 1260–1269.
51. Kumar, V.; Ranga Raju, K.G.; Vittal, N. Reduction of local scour around bridge piers using slot and collar. *J. Hydraul. Eng.* **1999**, *125*, 1302–1305. https://doi.org/10.1061/(ASCE)0733-9429(1999)125:12(1302).
52. Murtaza, N.; Khan, Z.U.; Khedher, K.M.; Amir, R.A.; Khan, D.; Salem, M.A.; Alsulamy, S. Mitigating scour at bridge abutments: An experimental investigation of waste material as an eco-friendly solution. *Water* **2023**, *15*, 3798. https://doi.org/10.3390/w15213798.
53. Choi, D.K. Data-driven materials modeling with XGBoost algorithm and statistical inference analysis for prediction of fatigue strength of steels. *Int. J. Precis. Eng. Manuf.* **2019**, *20*, 129–138. https://doi.org/10.1007/s12541-019-00048-6.
54. Minsky, M.L.; Papert, S.A. *Perceptrons, Expanded Edition*; The MIT Press: Cambridge, MA, USA, 1988.
55. Bento, C. Multilayer Perceptron Explained with a Real-Life Example and Python Code: Sentiment Analysis. Towards Data Science. 2021. Available online: https://towardsdatascience.com/multilayer-perceptron-explained-with-a-real-life-example-and-python-code-sentiment-analysis-cb408ee93141(accessed on 21 September 2021).
56. Müller, A.C.; Guido, S. *Introduction to Machine Learning with Python: A guide for Data Scientists*; O'Reilly Media, Inc.: Sebastopol, CA, USA, 2016.
57. Hastie, T.; Tibshirani, R.; Friedman, J.H. *The Elements of Statistical Learning: Data Mining, Inference, and Prediction*, 2th ed.; Springer: New York, NY, USA, 2009; pp. 1–758.
58. Ceperic, E.; Ceperic, V.; Baric, A. A strategy for short-term load forecasting by support vector regression machines. *IEEE Trans. Power Syst.*, **2013**, *28*, 4356–4364. https://doi.org/10.1109/tpwrs.2013.2269803.
59. Géron, A. *Hands-on Machine Learning with Scikit-Learn, Keras, and TensorFlow*; O'Reilly Media, Inc.: Sebastopol, CA, USA, 2022.